



The Atacama Cosmology Telescope: A Catalog of >4000 Sunyaev–Zel’dovich Galaxy Clusters

M. Hilton^{1,2} , C. Sifón³ , S. Naess⁴, M. Madhavacheril⁵ , M. Oguri^{6,7,8} , E. Rozo⁹, E. Rykoff^{10,11} , T. M. C. Abbott¹², S. Adhikari^{10,11,13}, M. Aguena^{14,15}, S. Aiola⁴, S. Allam¹⁶, S. Amodeo¹⁷, A. Amon¹⁰, J. Annis¹⁶ , B. Ansarinejad¹⁸, C. Aros-Bunster³ , J. E. Austermann¹⁹, S. Avila²⁰, D. Bacon²¹, N. Battaglia¹⁷, J. A. Beall¹⁹, D. T. Becker¹⁹, G. M. Bernstein²² , E. Bertin^{23,24}, T. Bhandarkar²², S. Bhargava²⁵, J. R. Bond²⁶, D. Brooks²⁷ , D. L. Burke^{10,11}, E. Calabrese²⁸, M. Carrasco Kind^{29,30} , J. Carretero³¹ , S. K. Choi^{17,32}, A. Choi³³, C. Conselice^{34,35} , L. N. da Costa^{15,36}, M. Costanzi^{37,38} , D. Crichton^{1,2} , K. T. Crowley³⁹, R. Dünner⁴⁰, E. V. Denison¹⁹, M. J. Devlin²², S. R. Dicker²² , H. T. Diehl¹⁶ , J. P. Dietrich⁴¹ , P. Doel²⁷, S. M. Duff¹⁹, A. J. Duivenvoorden⁴², J. Dunkley^{42,43}, S. Everett⁴⁴, S. Ferraro^{45,46} , I. Ferrero⁴⁷, A. Ferte⁴⁸, B. Flaugher¹⁶ , J. Frieman^{16,49} , P. A. Gallardo³², J. García-Bellido²⁰ , E. Gaztanaga^{50,51} , D. W. Gerdes^{52,53} , P. Giles²⁵, J. E. Golec⁵⁴, M. B. Gralla⁵⁵, S. Grandis⁴¹, D. Gruen^{10,11,13} , R. A. Gruendl^{29,30} , J. Gschwend^{15,36} , G. Gutierrez¹⁶ , D. Han⁵⁶, W. G. Hartley^{27,57,58}, M. Hasselfield⁴, J. C. Hill^{4,59}, G. C. Hilton¹⁹, A. D. Hincks⁶⁰ , S. R. Hinton⁶¹ , S.-P. P. Ho⁴², K. Honscheid^{33,62} , B. Hoyle^{41,63,64} , J. Hubmayr¹⁹, K. M. Huffenberger⁶⁵ , J. P. Hughes⁶⁶ , A. T. Jaelani^{67,68}, B. Jain²², D. J. James⁶⁹ , T. Jeltema⁴⁴, S. Kent^{16,49}, K. Knowles^{1,2}, B. J. Koopman⁷⁰, K. Kuehn^{71,72} , O. Lahav²⁷ , M. Lima^{14,15}, Y.-T. Lin⁷³, M. Lokken^{26,60,74}, S. I. Loubser⁷⁵, N. MacCrann^{33,62}, M. A. G. Maia^{15,36} , T. A. Marriage⁷⁶, J. Martin⁷⁷, J. McMahon^{49,53,54,78,79}, P. Melchior⁴³ , F. Menanteau^{29,30} , R. Miquel^{31,80} , H. Miyatake^{8,81,82}, K. Moodley^{1,2} , R. Morgan⁸³, T. Mroczkowski⁸⁴ , F. Nati⁸⁵, L. B. Newburgh⁷⁰, M. D. Niemack^{17,32} , A. J. Nishizawa⁸⁶ , R. L. C. Ogando^{15,36} , J. Orlowski-Scherer²², L. A. Page⁴², A. Palmese^{16,49} , B. Partridge⁸⁷, F. Paz-Chinchón^{30,88}, P. Phakathi^{1,2}, A. A. Plazas⁴³ , N. C. Robertson^{89,90}, A. K. Romer²⁵ , A. Carnero Rosell^{91,92} , M. Salatino^{10,13}, E. Sanchez⁹³ , E. Schaan^{45,46}, A. Schillaci⁹⁴, N. Sehgal⁵⁶ , S. Serrano^{50,51}, T. Shin²², S. M. Simon¹⁶, M. Smith⁹⁵, M. Soares-Santos⁵³ , D. N. Spergel^{4,43} , S. T. Staggs⁴², E. R. Storer⁴², E. Suchyta⁹⁶ , M. E. C. Swanson³⁰, G. Tarle⁵³ , D. Thomas²¹, C. To^{10,11,13} , H. Trac⁹⁷ , J. N. Ullom¹⁹, L. R. Vale¹⁹, J. Van Lanen¹⁹, E. M. Vavagiakis³², J. De Vicente⁹³ , R. D. Wilkinson²⁵, E. J. Wollack⁹⁸ , Z. Xu²² , and Y. Zhang¹⁶

¹ Astrophysics Research Centre, University of KwaZulu-Natal, Westville Campus, Durban 4041, South Africa; hiltonm@ukzn.ac.za

² School of Mathematics, Statistics & Computer Science, University of KwaZulu-Natal, Westville Campus, Durban 4041, South Africa

³ Instituto de Física, Pontificia Universidad Católica de Valparaíso, Casilla 4059, Valparaíso, Chile

⁴ Center for Computational Astrophysics, Flatiron Institute, New York, NY 10010, USA

⁵ Centre for the Universe, Perimeter Institute for Theoretical Physics, Waterloo, ON, N2L 2Y5, Canada

⁶ Research Center for the Early Universe, University of Tokyo, Tokyo 113-0033, Japan

⁷ Department of Physics, University of Tokyo, Tokyo 113-0033, Japan

⁸ Kavli Institute for the Physics and Mathematics of the Universe (Kavli IPMU, WPI), University of Tokyo, Chiba 277-8582, Japan

⁹ Department of Physics, University of Arizona, Tucson, AZ 85721, USA

¹⁰ Kavli Institute for Particle Astrophysics & Cosmology, P.O. Box 2450, Stanford University, Stanford, CA 94305, USA

¹¹ SLAC National Accelerator Laboratory, Menlo Park, CA 94025, USA

¹² Cerro Tololo Inter-American Observatory, NSF’s National Optical-Infrared Astronomy Research Laboratory, Casilla 603, La Serena, Chile

¹³ Department of Physics, Stanford University, 382 Via Pueblo Mall, Stanford, CA 94305, USA

¹⁴ Departamento de Física Matemática, Instituto de Física, Universidade de São Paulo, CP 66318, São Paulo, SP, 05314-970, Brazil

¹⁵ Laboratório Interinstitucional de e-Astronomia—LInEA, Rua Gal. José Cristino 77, Rio de Janeiro, RJ—20921-400, Brazil

¹⁶ Fermi National Accelerator Laboratory, P.O. Box 500, Batavia, IL 60510, USA

¹⁷ Department of Astronomy, Cornell University, Ithaca, NY 14853, USA

¹⁸ Department of Physics, Durham University, South Road, Durham DH1 3LE, UK

¹⁹ Quantum Sensors Group, NIST, 325 Broadway, Boulder, CO 80305, USA

²⁰ Instituto de Física Teórica UAM/CSIC, Universidad Autónoma de Madrid, E-28049 Madrid, Spain

²¹ Institute of Cosmology and Gravitation, University of Portsmouth, Portsmouth, PO1 3FX, UK

²² Department of Physics and Astronomy, University of Pennsylvania, Philadelphia, PA 19104, USA

²³ CNRS, UMR 7095, Institut d’Astrophysique de Paris, F-75014, Paris, France

²⁴ Sorbonne Universités, UPMC Univ Paris 06, UMR 7095, Institut d’Astrophysique de Paris, F-75014, Paris, France

²⁵ Department of Physics and Astronomy, Pevsey Building, University of Sussex, Brighton, BN1 9QH, UK

²⁶ Canadian Institute for Theoretical Astrophysics, University of Toronto, Toronto, ON, M5S 3H8, Canada

²⁷ Department of Physics & Astronomy, University College London, Gower Street, London, WC1E 6BT, UK

²⁸ School of Physics and Astronomy, Cardiff University, The Parade, Cardiff, Wales, CF24 3AA, UK

²⁹ Department of Astronomy, University of Illinois at Urbana-Champaign, 1002 W. Green Street, Urbana, IL 61801, USA

³⁰ National Center for Supercomputing Applications, 1205 West Clark St., Urbana, IL 61801, USA

³¹ Institut de Física d’Altes Energies (IFAE), The Barcelona Institute of Science and Technology, Campus UAB, E-08193 Bellaterra (Barcelona) Spain

³² Department of Physics, Cornell University, Ithaca, NY 14853, USA

³³ Center for Cosmology and Astro-Particle Physics, The Ohio State University, Columbus, OH 43210, USA

³⁴ Jodrell Bank Center for Astrophysics, School of Physics and Astronomy, University of Manchester, Oxford Road, Manchester, M13 9PL, UK

³⁵ University of Nottingham, School of Physics and Astronomy, Nottingham NG7 2RD, UK

³⁶ Observatório Nacional, Rua Gal. José Cristino 77, Rio de Janeiro, RJ—20921-400, Brazil

³⁷ INAF-Osservatorio Astronomico di Trieste, via G.B. Tiepolo 11, I-34143 Trieste, Italy

³⁸ Institute for Fundamental Physics of the Universe, Via Beirut 2, I-34014 Trieste, Italy

³⁹ Department of Physics, University of California, Berkeley, 366 LeConte Hall, Berkeley, CA 94720, USA

⁴⁰ Instituto de Astrofísica and Centro de Astro-Ingeniería, Facultad de Física, Pontificia Universidad Católica de Chile, Av. Vicuña Mackenna 4860, 7820436, Macul, Santiago, Chile

⁴¹ Faculty of Physics, Ludwig-Maximilians-Universität, Scheinerstr. 1, D-81679 Munich, Germany

- ⁴² Joseph Henry Laboratories of Physics, Jadwin Hall, Princeton University, Princeton, NJ 08544, USA
⁴³ Department of Astrophysical Sciences, Princeton University, Peyton Hall, Princeton, NJ 08544, USA
⁴⁴ Santa Cruz Institute for Particle Physics, Santa Cruz, CA 95064, USA
⁴⁵ Lawrence Berkeley National Laboratory, One Cyclotron Road, Berkeley, CA 94720, USA
⁴⁶ Berkeley Center for Cosmological Physics, UC Berkeley, CA 94720, USA
⁴⁷ Institute of Theoretical Astrophysics, University of Oslo, P.O. Box 1029 Blindern, NO-0315 Oslo, Norway
⁴⁸ Jet Propulsion Laboratory, California Institute of Technology, 4800 Oak Grove Dr., Pasadena, CA 91109, USA
⁴⁹ Kavli Institute for Cosmological Physics, University of Chicago, Chicago, IL 60637, USA
⁵⁰ Institut d'Estudis Espacials de Catalunya (IEEC), E-08034 Barcelona, Spain
⁵¹ Institute of Space Sciences (ICE, CSIC), Campus UAB, Carrer de Can Magrans, s/n, E-08193 Barcelona, Spain
⁵² Department of Astronomy, University of Michigan, Ann Arbor, MI 48109, USA
⁵³ Department of Physics, University of Michigan, Ann Arbor, MI 48109, USA
⁵⁴ Department of Physics, University of Chicago, Chicago, IL 60637, USA
⁵⁵ Department of Astronomy/Steward Observatory, University of Arizona, 933 N Cherry Ave, Tucson, AZ 85719, USA
⁵⁶ Physics and Astronomy Department, Stony Brook University, Stony Brook, NY 11794, USA
⁵⁷ Département de Physique Théorique and Center for Astroparticle Physics, Université de Genève, 24 quai Ernest Ansermet, CH-1211 Geneva, Switzerland
⁵⁸ Department of Physics, ETH Zurich, Wolfgang-Pauli-Strasse 16, CH-8093 Zurich, Switzerland
⁵⁹ Department of Physics, Columbia University, New York, NY 10027, USA
⁶⁰ David A. Dunlap Department of Astronomy and Astrophysics, University of Toronto, 50 St George Street, Toronto, ON, M5S 3H4, Canada
⁶¹ School of Mathematics and Physics, University of Queensland, Brisbane, QLD 4072, Australia
⁶² Department of Physics, The Ohio State University, Columbus, OH 43210, USA
⁶³ Max Planck Institute for Extraterrestrial Physics, Giessenbachstrasse, D-85748 Garching, Germany
⁶⁴ Universitäts-Sternwarte, Fakultät für Physik, Ludwig-Maximilians Universität München, Scheinerstr. 1, D-81679 München, Germany
⁶⁵ Department of Physics, Florida State University, Tallahassee FL 32306, USA
⁶⁶ Department of Physics and Astronomy, Rutgers, The State University of New Jersey, Piscataway, NJ 08854-8019, USA
⁶⁷ Department of Physics, Kindai University, 3-4-1 Kowakae, Higashi-Osaka, Osaka 577-8502, Japan
⁶⁸ Astronomy Research Division and Bosscha Observatory, FMIPA, Institut Teknologi Bandung, Jl. Ganesha 10, Bandung 40132, Indonesia
⁶⁹ Center for Astrophysics | Harvard & Smithsonian, 60 Garden Street, Cambridge, MA 02138, USA
⁷⁰ Department of Physics, Yale University, 217 Prospect St, New Haven, CT 06511, USA
⁷¹ Australian Astronomical Optics, Macquarie University, North Ryde, NSW 2113, Australia
⁷² Lowell Observatory, 1400 Mars Hill Rd, Flagstaff, AZ 86001, USA
⁷³ Institute of Astronomy and Astrophysics, Academia Sinica, Taipei 10617, Taiwan
⁷⁴ Dunlap Institute for Astronomy and Astrophysics, University of Toronto, 50 St. George St., Toronto, ON, M5S 3H4, Canada
⁷⁵ Centre for Space Research, North-West University, Potchefstroom 2520, South Africa
⁷⁶ Department of Physics and Astronomy, Johns Hopkins University, 3400 N. Charles St., Baltimore, MD 21218, USA
⁷⁷ Half Hollow Hills High School East, 50 Vanderbilt Pkwy, Dix Hills, NY 11746, USA
⁷⁸ Department of Astronomy and Astrophysics, University of Chicago, 5640 S. Ellis Ave., Chicago, IL 60637, USA
⁷⁹ Enrico Fermi Institute, University of Chicago, Chicago, IL 60637, USA
⁸⁰ Institució Catalana de Recerca i Estudis Avançats, E-08010 Barcelona, Spain
⁸¹ Institute for Advanced Research, Nagoya University, Nagoya 464-8601, Japan
⁸² Division of Particle and Astrophysical Science, Graduate School of Science, Nagoya University, Nagoya 464-8602, Japan
⁸³ Physics Department, 2320 Chamberlin Hall, University of Wisconsin-Madison, 1150 University Avenue Madison, WI 53706-1390, USA
⁸⁴ European Southern Observatory (ESO), Karl-Schwarzschild-Strasse 2, Garching, D-85748, Germany
⁸⁵ Department of Physics, University of Milano-Bicocca, Piazza della Scienza 3, I-20126 Milano (MI), Italy
⁸⁶ Institute for Advanced Research, Nagoya University, Furocho, Chikusa, Nagoya, Aichi 464-8602, Japan
⁸⁷ Department of Physics and Astronomy, Haverford College, Haverford, PA 19041, USA
⁸⁸ Institute of Astronomy, University of Cambridge, Madingley Road, Cambridge CB3 0HA, UK
⁸⁹ Institute of Astronomy, Madingley Road, Cambridge, CB3 0HA, UK
⁹⁰ Kavli Institute for Cosmology Cambridge, Madingley Road, Cambridge, CB3 0HA, UK
⁹¹ Instituto de Astrofísica de Canarias, E-38205 La Laguna, Tenerife, Spain
⁹² Universidad de La Laguna, Dpto. Astrofísica, E-38206 La Laguna, Tenerife, Spain
⁹³ Centro de Investigaciones Energéticas, Medioambientales y Tecnológicas (CIEMAT), Madrid, Spain
⁹⁴ Department of Physics, California Institute of Technology, Pasadena, CA 91125, USA
⁹⁵ School of Physics and Astronomy, University of Southampton, Southampton, SO17 1BJ, UK
⁹⁶ Computer Science and Mathematics Division, Oak Ridge National Laboratory, Oak Ridge, TN 37831, USA
⁹⁷ McWilliams Center for Cosmology, Department of Physics, Carnegie Mellon University, Pittsburgh, PA 15213, USA
⁹⁸ NASA/Goddard Space Flight Center, Greenbelt, MD 20771, USA

Received 2020 September 23; revised 2020 December 1; accepted 2020 December 1; published 2021 February 16

Abstract

We present a catalog of 4195 optically confirmed Sunyaev–Zel’dovich (SZ) selected galaxy clusters detected with signal-to-noise ratio >4 in $13,211 \text{ deg}^2$ of sky surveyed by the Atacama Cosmology Telescope (ACT). Cluster candidates were selected by applying a multifrequency matched filter to 98 and 150 GHz maps constructed from ACT observations obtained from 2008 to 2018 and confirmed using deep, wide-area optical surveys. The clusters span the redshift range $0.04 < z < 1.91$ (median $z = 0.52$). The catalog contains 222 $z > 1$ clusters, and a total of 868 systems are new discoveries. Assuming an SZ signal versus mass-scaling relation calibrated from X-ray observations, the sample has a 90% completeness mass limit of $M_{500c} > 3.8 \times 10^{14} M_{\odot}$, evaluated at $z = 0.5$, for clusters detected at signal-to-noise ratio >5 in maps filtered at an angular scale of 2.4 . The survey has a large overlap with deep optical weak-lensing surveys that are being used to calibrate the SZ signal mass-scaling relation, such as the Dark Energy Survey (4566 deg^2), the Hyper Suprime-Cam Subaru Strategic Program (469 deg^2), and the Kilo Degree Survey (825 deg^2). We highlight some noteworthy objects in the sample, including potentially projected systems, clusters with strong lensing features, clusters with active central galaxies or star formation, and

systems of multiple clusters that may be physically associated. The cluster catalog will be a useful resource for future cosmological analyses and studying the evolution of the intracluster medium and galaxies in massive clusters over the past 10 Gyr.

Unified Astronomy Thesaurus concepts: [Galaxy clusters \(584\)](#); [Cosmology \(343\)](#); [Large-scale structure of the universe \(902\)](#)

Supporting material: FITS files

1. Introduction

The thermal Sunyaev–Zel’dovich effect (SZ; e.g., Sunyaev & Zel’dovich 1970; Sunyaev & Zeldovich 1972) is well established as a method for constructing approximately mass-limited samples of galaxy clusters, independently of redshift. The SZ effect arises through the inverse Compton scattering of cosmic microwave background (CMB) photons by electrons within the hot gas atmospheres of galaxy clusters (see reviews by Birkinshaw 1999; Carlstrom et al. 2002; Mroczkowski et al. 2019). This leads to a spectral distortion in sight lines toward clusters, such that at frequencies below 220 GHz, clusters appear as “cold spots” in the millimeter-wave sky, while at frequencies above 220 GHz, they appear as “hot spots.” The amplitude of the SZ signal scales with the mass of the cluster.

The unique power of SZ-selected cluster surveys to detect all of the massive structures in the universe regardless of their distance from the observer has driven the development of “blind” SZ surveys that constrain cosmological parameters by measuring the evolution of the cluster mass function (e.g., Vanderlinde et al. 2010; Sehgal et al. 2011; Hasselfield et al. 2013; Reichardt et al. 2013; Planck Collaboration et al. 2014a, 2016a; Bocquet et al. 2019). SZ cluster surveys over large areas of sky have been conducted by the South Pole Telescope (SPT; e.g., Williamson et al. 2011; Bleem et al. 2015b, 2020; Huang et al. 2020a), the Planck satellite mission (Planck Collaboration et al. 2014b, 2016b), and the Atacama Cosmology Telescope (ACT; Marriage et al. 2011; Hasselfield et al. 2013; Hilton et al. 2018). Collectively, since the first blind SZ detections by SPT (Staniszewski et al. 2009), these surveys have detected approximately 2300 clusters with redshift measurements to date.

In this paper, we present the first cluster catalog derived from observations using the Advanced ACTPol receiver (Henderson et al. 2016; Ho et al. 2017; Choi et al. 2018), combining this with all observations by ACT from 2008 to 2018 (Naess et al. 2020, N20 hereafter; details of previous generations of ACT instrumentation can be found in Fowler et al. 2007; Swetz et al. 2011; and Thornton et al. 2016). This is the first ACT cluster catalog to use multifrequency data (98 and 150 GHz) in its construction. The SZ cluster search area covers 13,211 deg², and we have optically confirmed and measured redshifts for 4195 clusters out of 8878 candidates detected with signal-to-noise ratio (S/N) > 4. The cluster catalog is publicly available in FITS table format at the NASA Legacy Archive for Microwave Background Data (LAMBDA) as part of the fifth ACT data release (ACT DR5⁹⁹). Table 1 describes the contents of the catalog.

The structure of this paper is as follows. In Section 2, we describe the ACT maps used in this work, the SZ cluster-detection algorithm, and our process for estimating cluster masses from the SZ signal. In Section 3, we explain how we

optically confirmed SZ detections as galaxy clusters and assigned their redshifts, making use of deep wide-area optical/IR surveys in conjunction with our own follow-up observations. In Section 4, we present the statistical properties of the cluster catalog and compare it with previous work by the ACT collaboration. We discuss our catalog in comparison with other cluster samples in Section 5. We present a summary in Section 6.

We assume a flat cosmology with $\Omega_m = 0.3$, $\Omega_\Lambda = 0.7$, and $H_0 = 70 \text{ km s}^{-1} \text{ Mpc}^{-1}$ throughout. We quote cluster mass estimates (M_{500c}) within a spherical radius that encloses an average density equal to 500 times the critical density at the cluster redshift (R_{500c}). All magnitudes are on the AB system (Oke 1974), unless stated otherwise.

2. ACT Observations and SZ Cluster Candidate Selection

2.1. 98 and 150 GHz Observations and Maps

The ACT experiment saw first light in 2007, and since 2016 it has been observing with its third-generation receiver, Advanced ACTPol (AdvACT; Henderson et al. 2016). AdvACT consists of three detector arrays containing dichroic, dual polarization horn-coupled Transition Edge Sensor (TES) bolometers, observing at 98, 150, and 220 GHz, with 27 and 39 GHz channels added in the 2020 season. For this work, we use data from only the 98 and 150 GHz channels, which have approximate beam FWHM 2'2 and 1'4, respectively.

The cluster search was performed on coadded maps containing ACT data obtained between 2008 and 2018 (made available to the community as ACT DR5). The ACT maps for the 2008–2016 observing seasons are publicly available on the LAMBDA website, with seasons 2013–2016 being processed for ACT DR4 (Aiola et al. 2020; Choi et al. 2020). ACT DR5 contains coadded maps that incorporate early versions of the 2017–2018 data (N20) and, unlike previous ACT data releases, includes observations taken during daylight hours. These maps have not been subjected to the full battery of tests needed for precision measurements of the CMB power spectrum, and they may contain gain errors at the level of a few percent. They are, however, much deeper over a much wider area than the maps used in the ACT DR4 analysis. More than 12,000 deg² (91% of the 13,211 deg² cluster search area) has noise level <30 μK -arcmin at 150 GHz (N20).

The coadded maps used in this work were produced in a two-step procedure (described in detail in N20). Individual maximum-likelihood maps were first made for each observing season, frequency, and detector array, following the procedures described in Dünner et al. (2013) and Aiola et al. (2020). These maps were then combined into a single map per frequency, convolved to a common beam, by breaking each map into a series of tiles and weighting by a noise model constructed from the hitcount-modulated 2D noise power spectrum for each tile.

The coadded maps cover a sky area of approximately 18,000 deg². However, several thousand square degrees

⁹⁹ https://lambda.gsfc.nasa.gov/product/act/actpol_prod_table.cfm

Table 1
Description of the Columns in the FITS Table Format Cluster Catalog, Available from LAMBDA (https://lambda.gsfc.nasa.gov/product/act/actpol_prod_table.cfm)

Column	Symbol	Description
name	...	Cluster name in the format ACT-CL JHHMM.m \pm DDMM
RAdeg	...	R.A. in decimal degrees (J2000) of the SZ detection by ACT
decDeg	...	Decl. in decimal degrees (J2000) of the SZ detection by ACT
SNR	S/N	Signal-to-noise ratio, optimized over all filter scales
y_c	y ₀	Central Comptonization parameter (10^{-4}) measured using the optimal matched filter template (i.e., the one that maximizes S/N). Uncertainty column(s): <code>err_y_c</code>
fixed_SNR	S/N _{2,4}	Signal-to-noise ratio at the reference 2/4 filter scale
fixed_y_c	\bar{y}_0	Central Comptonization parameter (10^{-4}) measured at the reference filter scale (2/4). Uncertainty column(s): <code>fixed_err_y_c</code>
template	...	Name of the matched filter template resulting in the highest S/N detection of this cluster
tileName	...	Name of the ACT map tile (typically with dimensions 10 deg \times 5 deg) in which the cluster was found
redshift	z	Adopted redshift for the cluster. The uncertainty is only given for photometric redshifts. Uncertainty column(s): <code>redshiftErr</code>
redshiftType	...	Redshift type (<code>spec</code> = spectroscopic, <code>phot</code> = photometric)
redshiftSource	...	Source of the adopted redshift (see Table 2)
M500c	M_{500c}^{UPP}	M_{500c} in units of $10^{14} M_{\odot}$, assuming the UPP and Arnaud et al. (2010) scaling relation to convert SZ signal to mass. Uncertainty column(s): <code>M500c_errPlus</code> , <code>M500c_errMinus</code>
M500cCal	M_{500c}^{Cal}	M_{500c} in units of $10^{14} M_{\odot}$, rescaled using the richness-based weak-lensing mass calibration factor of 0.71 ± 0.07 (see Section 4.1). Uncertainty column(s): <code>M500cCal_errPlus</code> , <code>M500cCal_errMinus</code>
M200m	M_{200m}^{UPP}	M_{200} with respect to the mean density, in units of $10^{14} M_{\odot}$, converted from M_{500c} using the Bhattacharya et al. (2013) c-M relation. Uncertainty column(s): <code>M200m_errPlus</code> , <code>M200m_errMinus</code>
M500cUncorr	M_{500c}^{Unc}	M_{500c} in units of $10^{14} M_{\odot}$, assuming the UPP and Arnaud et al. (2010) scaling relation to convert SZ signal to mass, uncorrected for bias due to the steepness of the cluster mass function and intrinsic scatter. Uncertainty column(s): <code>M500cUncorr_errPlus</code> , <code>M500cUncorr_errMinus</code>
M200mUncorr	M_{200m}^{Unc}	M_{200} with respect to the mean density, in units of $10^{14} M_{\odot}$, converted from M_{500c} using the Bhattacharya et al. (2013) c-M relation, uncorrected for bias due to the steepness of the cluster mass function and intrinsic scatter. Uncertainty column(s): <code>M200mUncorr_errPlus</code> , <code>M200mUncorr_errMinus</code>
footprint_DESY3	...	Flag indicating if the cluster falls within the DES Y3 footprint
footprint_HSCs19a	...	Flag indicating if the cluster falls within the HSC-SSP S19A footprint (assuming the full-depth full-color HSC-SSP mask)
footprint_KiDSDR4	...	Flag indicating if the cluster falls within the KiDS DR4 footprint
zCluster_delta	δ	Density contrast statistic measured at the <code>zCluster</code> photometric redshift. Uncertainty column(s): <code>zCluster_errDelta</code>
zCluster_source	...	Photometry used for <code>zCluster</code> measurements (see Section 3.1.4). One of <code>DECaLS</code> (DR8), <code>KiDS</code> (DR4), <code>SDSS</code> (DR12)
RM	...	Flag indicating cross-match with a <code>redMaPPer</code> -detected cluster in the SDSS footprint (Rykoff et al. 2014)
RM_LAMBDA	λ	Optical richness measurement for the <code>redMaPPer</code> algorithm in the SDSS footprint. Uncertainty column(s): <code>RM_LAMBDA_ERR</code>
RMDESY3	...	Flag indicating cross-match with a <code>redMaPPer</code> -detected cluster in the DES Y3 footprint (for details of the <code>redMaPPer</code> algorithm applied to DES data, see Rykoff et al. 2016)
RMDESY3_LAMBDA_CHISQ	λ	Optical richness measurement for the <code>redMaPPer</code> algorithm in the DES Y3 footprint. Uncertainty column(s): <code>RMDESY3_LAMBDA_CHISQ_E</code>
CAMIRA	...	Flag indicating cross-match with a CAMIRA-detected cluster in the HSCSSP S19A footprint (for details of the CAMIRA algorithm, see Oguri 2014; Oguri et al. 2018)
CAMIRA_N_mem	...	Optical richness measurement for the CAMIRA algorithm in the HSCSSP S19A footprint
opt_RAdeg	...	Alternative optically determined R.A. in decimal degrees (J2000), from a heterogeneous collection of measurements (see <code>opt_positionSource</code>)
opt_decDeg	...	Alternative optically determined decl. in decimal degrees (J2000), from a heterogeneous collection of measurements (see <code>opt_positionSource</code>)
opt_positionSource	...	Indicates the source of the alternative optically determined cluster position. One of <code>AMICO</code> (position from the AMICO cluster finder; Maturi et al. 2019), <code>CAMIRA</code> (position from the CAMIRA cluster finder; Oguri et al. 2018), <code>RM</code> , <code>RMDESY3</code> , <code>RMDESY3ACT</code> (position from the <code>redMaPPer</code> cluster finder, in SDSS, DES Y3, or DES Y3 using the ACT position as a prior; Rykoff et al. 2014, 2016), <code>Vis-BCG</code> (brightest central galaxy (BCG) position from visual inspection of available optical/IR imaging; this work), <code>WHL2015</code> (position from Wen & Han 2015)
notes	...	If present, at least one of <code>AGN?</code> (central galaxy may have color or spectrum indicating it may host an AGN), <code>Lensing?</code> (cluster may show strong gravitational lensing features), <code>Merger?</code> (cluster may be a merger), <code>Star formation?</code> (a galaxy near the center may have blue colors, which might indicate star formation if it is not a line-of-sight projection). These notes are not comprehensive and merely indicate some systems that were identified as potentially interesting during visual inspection of the available optical/IR imaging.
knownLens	...	Names of known strong gravitational lenses within 2 Mpc projected distance of this cluster (comma delimited when there are multiple matches)
knownLensRefCode	...	Reference codes (comma delimited when there are multiple matches) corresponding to the entries in the <code>knownLens</code> field. See Table 3 to map between the codes used in this field and references to the corresponding lens catalog papers.
warnings	...	If present, a warning message related to the redshift measurement for this cluster (e.g., possible projected system)

Note. The Symbol column provides a mapping between column names and symbols used in the text and figures of this article. (This table is available in its entirety in FITS format.)

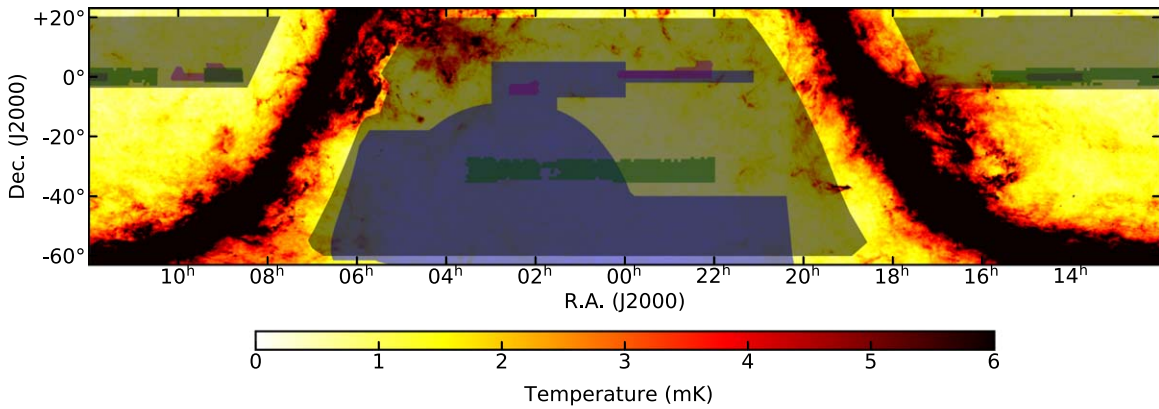


Figure 1. ACT DR5 cluster search area (shaded in gray; covering 13,211 deg² after masking), overlaid on the Planck 353 GHz map, which is sensitive to thermal emission by dust. The footprints of deep and wide optical surveys that will provide weak-lensing mass calibration of the cluster sample are highlighted: DES (blue), HSC (magenta), and KiDS (green).

correspond to low Galactic latitudes ($|b| < 20$ deg), where either the level of dust emission is high (making cluster detection in our millimeter-wave maps problematic) or the stellar density is high (making optical confirmation and redshift measurements difficult or impossible). Therefore, we defined the cluster search area (plotted over the Planck 353 GHz map in Figure 1) to exclude such regions. We also mask dusty regions within the cluster search region, defined as pixels with temperature > 0.004 K (in CMB temperature units) in the Planck 353 GHz map. We initially masked the locations of point sources detected in the ACT 150 GHz map using circular regions with radii in the range $3' - 12'$, depending on the amplitude of the source at 150 GHz. After visual inspection of the filtered maps (see Section 3.2), we found it necessary to mask some regions that were not captured by the above procedures. Typically these were cases where our automated procedure to define source masking had not selected a large-enough masking radius. We subsequently masked the locations of all sources with 150 GHz flux density > 10 mJy (approximately 11,000 objects) using circles with radius $320''$, except for those sources located within $9'$ of bright clusters (with $\bar{y}_0 > 1 \times 10^{-4}$; \bar{y}_0 is our chosen SZ observable, defined in Section 2.3), which are not masked (because “ringing” around bright clusters can be detected as spurious sources). After masking, the cluster search area is 13,211 deg².

2.2. Cluster Detection

We search for clusters using a multifrequency matched filter (e.g., Melin et al. 2006; Williamson et al. 2011), applied to the 98 and 150 GHz maps,

$$\psi(k_x, k_y, \nu_i) = A \sum_j N_{ij}^{-1}(k_x, k_y) f_{SZ}(\nu_j) S(k_x, k_y, \nu_j). \quad (1)$$

where ψ is the filter, (k_x, k_y) denote the spatial frequencies in the horizontal and vertical directions in the maps, N is the noise covariance between the maps at different frequencies ν , S is a beam-convolved signal template, and A is a normalization factor chosen such that, when applied to a set of maps containing a beam-convolved cluster signal (in temperature units), the matched filter returns the central Comptonization parameter (see Section 2.3). We use the nonrelativistic form for

the spectral dependence of the SZ effect given by

$$f_{SZ} = x \frac{e^x + 1}{e^x - 1} - 4, \quad (2)$$

where $x = h\nu/k_B T_{\text{CMB}}$. We adopt 97.8 GHz and 149.6 GHz as the thermal SZ-weighted band centers for the 98 and 150 GHz maps analyzed here. These are the median values of the SZ-weighted band centers of the individual detector arrays; in practice, the effective band centers vary slightly by position on the sky—see the appendix of N20—with uncertainty ≈ 1 GHz on arcmin scales.

We use the map itself to form the noise covariance N , as the maps are dominated by the CMB on large scales and white noise on small scales, rather than by the thermal SZ signal. Note that the filter is 2D in Fourier space, in order to account for the anisotropic noise that arises from the scan pattern of ACT (e.g., Marriage et al. 2011), which varies according to position on the sky. However, the signal template S is axisymmetric. We fill holes in the map created by point-source masking (see Section 2.1) with a heavily smoothed version of the map itself prior to Fourier transforming.

As in previous ACT cluster searches (Hasselfield et al. 2013; Hilton et al. 2018), throughout this work we model the cluster signal using the universal pressure profile (UPP; Arnaud et al. 2010, A10 hereafter), which is convolved with the appropriate ACT beam for each frequency to form the signal template S . To improve the detection efficiency for clusters with different angular sizes, we create a set of 16 matched filters, corresponding to $M_{500c} \in \{(1, 2, 4, 8) \times 10^{14} M_\odot\}$ and $z \in \{0.2, 0.4, 0.8, 1.2\}$.

The ACT maps cover approximately 18,000 deg², and the noise level in the maps varies considerably as a function of position on the sky (see Figure 2). In addition, the maps are produced in plate carrée projection (CAR in the terminology of FITS world coordinate systems; Calabretta & Greisen 2002), which leads to distortion away from the celestial equator as the solid angle covered by a pixel changes with decl. Therefore, we break the maps into a set of 280 tiles, each with approximate dimensions 10 deg \times 5 deg (R.A. \times decl.) and construct a different set of matched filters for each tile. Figure 2 shows the layout of the tiles on the 150 GHz white noise level map (as produced by the map maker). Since we apodize each tile before Fourier transforming when constructing N , each tile is extended with a one-degree-wide border that overlaps its neighbors.

To select cluster candidates, we construct an S/N map for each filtered tile and, in turn, make a segmentation map that

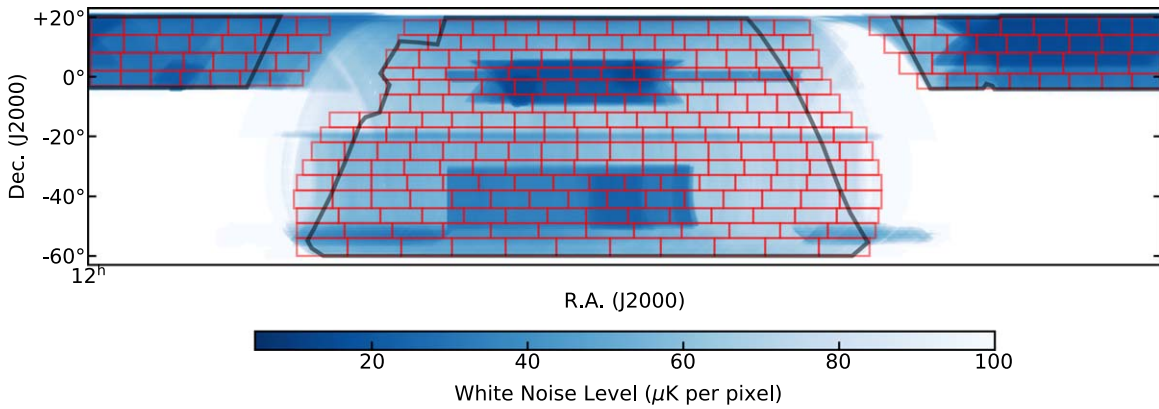


Figure 2. Map of the white noise level in the 150 GHz map, as produced by the map maker. The 98 and 150 GHz maps, which cover 18,000 deg² in total, are broken into tiles (marked in red) before filtering, for the reasons outlined in Section 2.2. The black outline marks the cluster search region, before the dust and point-source masks are applied.

identifies peaks with $S/N > 4$. We estimate the noise map in a way similar to that used in Hilton et al. (2018), by dividing each tile into square 40' cells and measuring the 3σ -clipped standard deviation in each cell, taking into account masked regions.¹⁰⁰ This accounts for variations in depth within each tile. Finally, we apply the cluster search area mask shown in Figure 1 and apply the dust and point-source masks (see Section 2.1). Figure 3 shows a comparison between the unfiltered 98 and 150 GHz maps and a filtered map, after the application of all of the above procedures.

We assemble the final catalog of cluster candidates from a set of catalogs extracted from each S/N map for each filter scale in each tile, using a procedure similar to Hilton et al. (2018). We use a minimum detection threshold of a single pixel with $S/N > 4$ in any filtered map, and we adopt the location of the center of mass of the $S/N > 4$ pixels in each detected object in the filtered map as the coordinates of each cluster candidate. We then create a final master candidate list by cross-matching the catalogs assembled at each cluster scale using a 1/4 matching radius. Objects in the regions that overlap between tiles are removed by applying a mask; the tiles are defined such that each nonoverlapping pixel in a tile maps to a unique pixel in the pixelization of the original monolithic map. We adopt the maximum S/N across all filter scales for each candidate as the “optimal” S/N detection. However, as in Hasselfield et al. (2013) and Hilton et al. (2018), we also use a single reference filter scale (chosen to be $\theta_{500c} = 2.4$; see Section 2.3) at which we measure the cluster SZ signal and S/N. Throughout this work, we use S/N to refer to the “optimal” S/N (maximized over all filter scales) and $S/N_{2.4}$ for the S/N measured at the fixed 2.4 filter scale. The final catalog contains 8878 $S/N > 4$ candidates selected from a survey area of 13,211 deg².

We checked the accuracy of recovered cluster positions by injecting simulated clusters into the maps and rerunning the filtering and cluster-detection procedures, taking care to remove objects corresponding to real cluster candidates from the resulting catalogs. The injected clusters are UPP models with uniformly distributed amplitudes and sizes selected from $\theta_{500c} (')$ $\in \{7.8, 4.2, 2.4, 1.5\}$. More than 5.7 million model clusters with $4 < S/N_{2.4} < 20$ are recovered from these simulations. We fit a

model of the form

$$r = Ae^{-S/N_{2.4}/B} + C, \quad (3)$$

where r specifies the distance (in arcmin) between input and recovered model cluster positions within which some percentile of the objects are found, and A , B , and C are fit parameters. Figure 4 shows this model plotted over the position recovery data for the 50, 95, and 99.7 percentiles. The radial distance within which 99.7% of the model clusters are recovered is specified by a model with $A = 38.1$, $B = 1.16$, and $C = 0.69$. We use this model for cross-matching cluster candidates against external catalogs (see Section 3.2). Note that the accuracy of position recovery depends on the cluster scale, with larger-scale clusters having less accurately recovered positions, but for our purposes an average over several scales is sufficient.

For some applications (e.g., stacking on cluster positions), it is useful to model the positional uncertainty using the Rayleigh distribution,

$$P(r, \sigma_R) = \frac{r}{\sigma_R} \exp(-r^2/2\sigma_R^2), \quad (4)$$

where r is the distance between the true and recovered cluster positions, and σ_R is the scale parameter for the distribution. We fitted models of the form given in Equation (4) to the distribution of recovered position offsets obtained from the source insertion simulations described above, binned by $S/N_{2.4}$. Figure 5 shows the resulting measurements of σ_R as a function of $S/N_{2.4}$, together with a simple model that captures how σ_R changes with $S/N_{2.4}$.

We assess the number of false-positive detections in the candidate list as a function of $S/N_{2.4}$ by running the cluster-detection algorithm over sky simulations that are free of cluster signal. We use the map-based simulations¹⁰¹ developed for Simons Observatory (Ade et al. 2019) for this purpose (A. Zonca et al. 2021, in preparation). We create maps at 93 and 145 GHz (the available bandpasses in the simulations are slightly different from ACT) on the N20 pixelization, containing a realization of the CMB plus the cosmic infrared background (CIB) as implemented in WebSky¹⁰² (Stein et al. 2020). Since a complete model suitable for generating random realizations of the noise in

¹⁰⁰ This method can underestimate the noise level within a 40' cell if it straddles an abrupt, large change in the map depth, resulting in spurious candidates along such features. This can be corrected by binning the filtered maps according to the weight maps produced by the map maker and will be implemented for the next version of the catalog.

¹⁰¹ https://github.com/simonsobs/map_based_simulations/

¹⁰² https://mocks.cita.utoronto.ca/index.php/WebSky_Extragalactic_CMB_Mocks

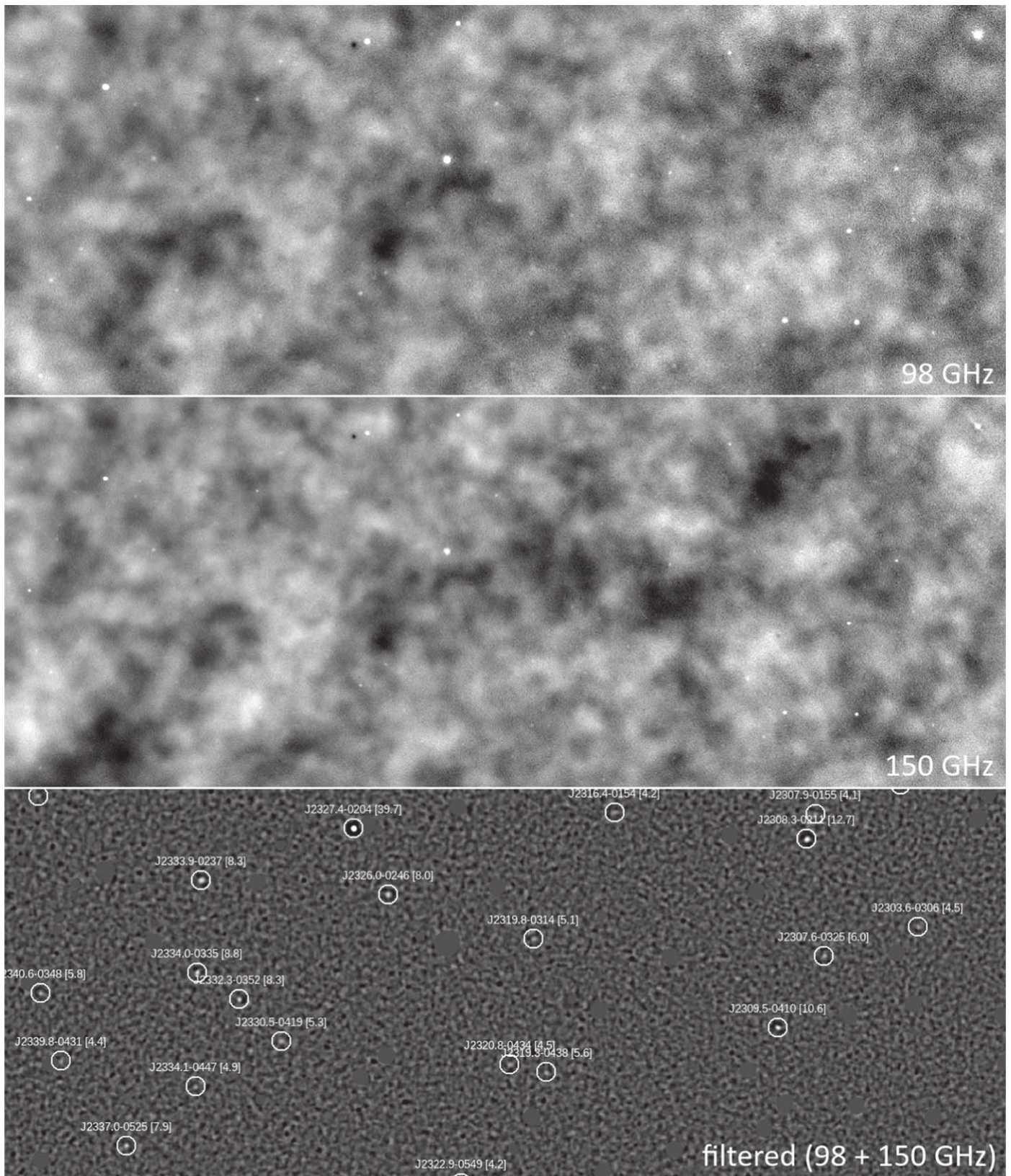


Figure 3. Comparison between the unfiltered 98 and 150 GHz maps and the filtered S/N map, for an approximately $10 \text{ deg} \times 4 \text{ deg}$ patch of sky. In the unfiltered maps, clusters appear as decrements (dark spots) in the map. Point sources appear as white spots, and CMB fluctuations dominate at large angular scales. In the filtered S/N map, clusters appear as white spots (marked with white circles to guide the eye; the number given in brackets is $S/N_{2.4}$), and point sources have been masked. The brightest object visible is the $z = 0.70$ cluster ACT-CL J2327.4-0204 (center left, near the top left of the image), which is an $S/N_{2.4} = 39.7$ detection.

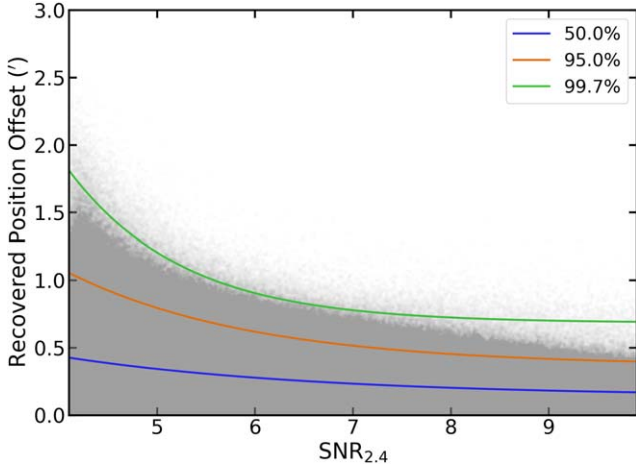


Figure 4. Accuracy of position recovery for injected UPP-model clusters as a function of $S/N_{2.4}$. The offset with respect to the original input cluster position is plotted on the vertical axis. The gray points show the offsets recovered for individual model clusters. The solid lines show model fits of the form given in Equation (3) that enclose the 50, 95, and 99.7 percentiles.

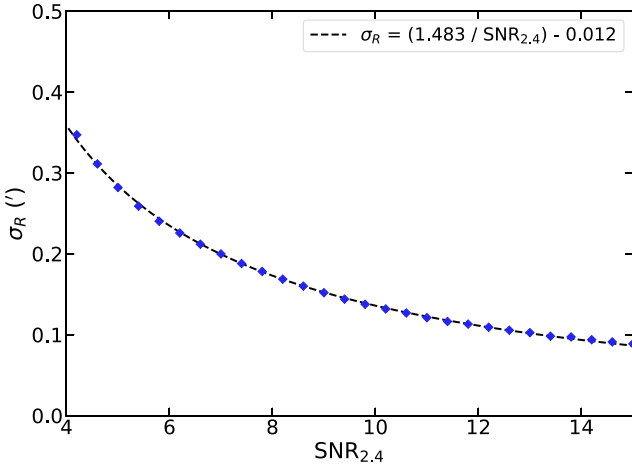


Figure 5. Results of fitting the distribution of recovered position offsets obtained from source insertion simulations using the Rayleigh distribution (Equation (4)). The simple model shown is a good description of how the scale parameter σ_R changes as a function of $S/N_{2.4}$.

the **N20** maps is not currently available (and there are no splits of the **N20** maps), we add white noise to the simulated maps following the levels in the **N20** inverse variance maps. This means that the false-positive rate inferred from these maps will be slightly optimistic, but as shown in Section 3.3, it is a reasonable match to the purity of the real cluster sample as assessed from regions with deep optical data. We apply all of the same masks to the signal-free simulated maps as are used on the real maps, so the resulting catalog is drawn from a simulated survey with exactly the same area as the real ACT DR5.

The upper panel of Figure 6 shows the number of detections in the signal-free simulation (N_{False}) as a function of $S/N_{2.4}$ cut. For $S/N_{2.4} > 4$, we find there are 2471 false detections, falling to 75 for $S/N_{2.4} > 5$ and 2 for $S/N_{2.4} > 6$. For comparison, there are 7407 $S/N_{2.4} > 4$ candidates in the real candidate list (note that the full candidate list is not provided with this paper; we release only the catalog of optically confirmed clusters). Assuming that N_{False} is a reasonable estimate of the false-positive rate in the real cluster candidate list, we can estimate the fraction of false positives as $F_{\text{False}} = N_{\text{False}}/N_{\text{Total}}$, where N_{Total} is the number of objects in the

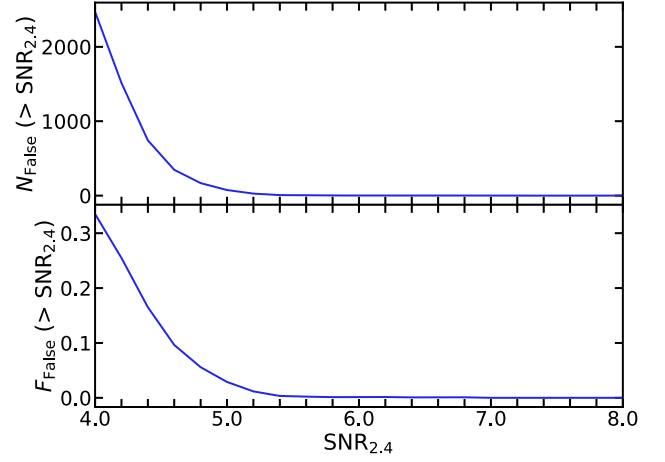


Figure 6. The number of false-positive detections (N_{False} ; upper panel) above a given $S/N_{2.4}$ cut resulting from running the cluster finder on signal-free simulated maps with the same survey area, masks, and pixelization as the real **N20** maps. The lower panel shows the fraction of false positives (F_{False}) expected in the real ACT DR5 candidate list above a given $S/N_{2.4}$ cut. As shown in Section 3.3, the simple simulations used here are a reasonable match to the fraction of clusters recovered in regions where deep optical observations are used for confirmation.

real ACT DR5 candidate list. This is shown in the lower panel of Figure 6. We find that $F_{\text{False}} = 0.34$ for $S/N_{2.4} > 4$, 0.03 for $S/N_{2.4} > 5$, and 0.001 for $S/N_{2.4} > 6$. Note that while these figures are a survey-wide average, we find little difference if we repeat this exercise considering only deeper parts of the map (e.g., F_{False} differs by $< 2\%$ if we compare the footprint that overlaps with HSCSSP, where the ACT observations are deepest, with the whole survey footprint). We caution that these figures represent lower limits to the contamination rate in the candidate list, as the simulations used here do not capture all of the possible noise sources in the real maps. We compare $1 - F_{\text{False}}$ to the fraction of optically confirmed clusters in Section 3.3.

2.3. Cluster Characterization

In this work, we continue to use the same approach to characterizing the SZ signal and its relation to mass as introduced in Hasselfield et al. (2013) and used in the ACTPOL cluster search (Hilton et al. 2018). Briefly, we choose to characterize the SZ signal and survey completeness by selecting a single reference filter scale of angular size $\theta_{500c} = 2'.4$, which corresponds to a UPP-model cluster with mass $M_{500c} = 2 \times 10^{14} M_{\odot}$ at $z = 0.4$ (close to the median redshift of the sample) for our fiducial cosmology. This avoids interfilter noise bias, where local noise variations (e.g., the presence of CMB cold spots near candidates) can affect estimates of the cluster signal (and size) based on the maximal S/N filter scale (see the discussion in Hasselfield et al. 2013). However, we note that because the cluster finder still maximizes S/N over location on the sky, there is still a small positive bias in the recovered S/N values ($\approx 7\%$ at $S/N_{2.4} = 4.0$; see, e.g., Vanderlinde et al. 2010).

For a map filtered at the fixed $2'.4$ reference scale, we assume that the cluster central Compton parameter \tilde{y}_0 is related to mass through

$$\tilde{y}_0 = 10^{A_0} E(z)^2 \left(\frac{M_{500c}}{M_{\text{pivot}}} \right)^{1+B_0} Q(\theta_{500c}) f_{\text{rel}}(M_{500c}, z), \quad (5)$$

where $10^{A_0} = 4.95 \times 10^{-5}$ is the normalization, $B_0 = 0.08$, $M_{\text{pivot}} = 3 \times 10^{14} M_{\odot}$, $Q(\theta_{500c})$ is the filter mismatch function ($\theta_{500c} = R_{500c}/D_A$, where D_A is the angular diameter distance), and f_{rel} is a relativistic correction. Here, $E(z)$ describes the evolution of the Hubble parameter with redshift: $E(z) = \sqrt{\Omega_m(1+z)^3 + \Omega_\Lambda}$. The parameter values for 10^{A_0} , B_0 , and M_{pivot} are equivalent to the A10 scaling relation, which was calibrated using X-ray observations. While this will typically result in masses that are lower than those calibrated against weak-lensing measurements (e.g., Miyatake et al. 2019, in the case of ACTPol), we choose to use the A10 relation here to ease comparison with our previous work. We also provide an alternative set of masses, rescaled via a richness-based weak-lensing calibration procedure, as described in Section 4.1.

The function $Q(\theta_{500c})$ in Equation (5) accounts for the mismatch between the size of a cluster with a different mass and redshift and the reference model used to define the matched filter (including the effect of the beam) and in turn \tilde{y}_0 (see Section 3.1 of Hasselfield et al. 2013; Section 2.3 of Hilton et al. 2018). Since we break the map into tiles and construct a filter for each tile (Section 2.2), each tile has its own $Q(\theta_{500c})$ function.

We implement the relativistic correction f_{rel} applied in Equation (5) differently in this work compared to previous ACT cluster surveys, which were based solely on 150 GHz data rather than the 98 and 150 GHz maps analyzed here. The size of f_{rel} depends on frequency and is up to 1% larger at 150 GHz than at 98 GHz for very massive clusters ($M_{500c} \approx 8 \times 10^{14} M_{\odot}$). We use the Arnaud et al. (2005) mass–temperature relation to convert M_{500c} to temperature at a given cluster redshift, and then we apply the formulae of Itoh et al. (1998) to calculate f_{rel} at each frequency. The filter ψ defined in Equation (1) returns the value \tilde{y}_0 when applied to a set of multifrequency maps, weighting the contribution of each map to the returned SZ signal according to both the spectral dependence of the SZ signal (Equation (2)) and the noise in the map. We use these weights, which differ from tile to tile, to estimate an average f_{rel} for each cluster. The overall impact of the relativistic correction is small (approximately 3% for the median mass of the ACT DR5 cluster sample).

Equation (5) cannot be inverted to obtain the mass M_{500c} , due to the steepness of the cluster mass function and the presence of intrinsic log-normal scatter σ_{int} in \tilde{y}_0 about the mean relation defined by Equation (5). We adopt $\sigma_{\text{int}} = 0.2$ throughout this work, based on the results of numerical simulations (see Hasselfield et al. 2013). Given a cluster redshift measurement, mass estimates are extracted by computing the posterior probability

$$P(M_{500c}|\tilde{y}_0, z) \propto P(\tilde{y}_0|M_{500c}, z)P(M_{500c}|z), \quad (6)$$

where $P(M_{500c}|z)$ is the halo mass function at redshift z , for which we use the fitting formulae of Tinker et al. (2008), as implemented in the Core Cosmology Library v2.1 (CCL¹⁰³; Chisari et al. 2019). We assume $\sigma_8 = 0.80$ for such calculations throughout this work. We account for the uncertainties on both z and \tilde{y}_0 in calculating $P(M_{500c}|\tilde{y}_0, z)$ and adopt the maximum of the $P(M_{500c}|\tilde{y}_0, z)$ distribution as the cluster M_{500c} estimate. The uncertainties quoted on these masses are 1σ error bars that do not take into account any uncertainty in the scaling relation parameters.

¹⁰³ <https://github.com/LSSTDESC/CCL>

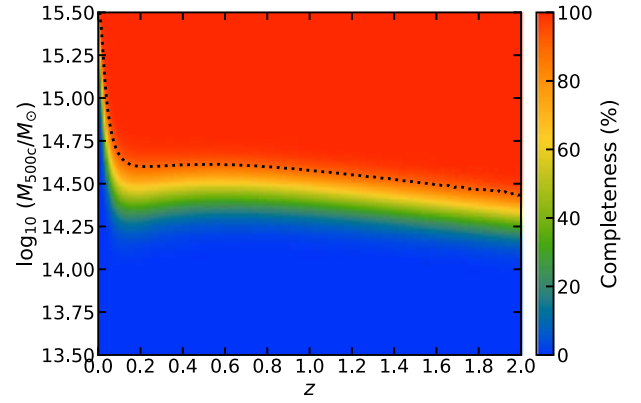


Figure 7. Completeness for $S/N_{2.4} > 5$ as a function of redshift, in terms of M_{500c}^{UPP} , over the full 13,211 deg^2 survey footprint. The Tinker et al. (2008) halo mass function and Arnaud et al. (2010) scaling relation are assumed (see Section 2.4). The dashed black contour marks the 90% completeness limit.

The mass estimates obtained through Equations (5) and (6) are referred to as M_{500c}^{UPP} throughout this work. For comparison with some other works (e.g., the Planck PSZ2 catalog; Planck Collaboration et al. 2016b), it is sometimes necessary to neglect the Eddington bias correction (done by Equation (6)) that accounts for the steepness of the cluster mass function and intrinsic scatter (see the discussion in Battaglia et al. 2016 and Hilton et al. 2018). We label these “uncorrected” masses as M_{500c}^{Unc} .

2.4. Survey Completeness

We estimate the completeness of the survey in terms of mass using mock catalogs generated through Monte Carlo simulations. For speed, the calculations are performed on a redshift grid covering the range $0 < z < 2$ in steps of size $\Delta z = 0.01$. At each redshift step, we make 2 million draws from the Tinker et al. (2008) halo mass function, above a minimum halo mass of $M_{500c} > 8 \times 10^{13} M_{\odot}$ (i.e., well below the expected mass limit). We then calculate the true value of \tilde{y}_0 for each of the randomly drawn halo masses using Equation (5), assuming the scaling relation parameters derived from A10. Here we apply the appropriate filter mismatch function (Q) for the tile each mock cluster is located in, and we apply the relativistic correction as described in Section 2.3. We then add Gaussian-distributed random noise to \tilde{y}_0 , according to the level estimated in the \tilde{y}_0 noise map, and finally we add log-normal scatter to \tilde{y}_0 with size $\sigma_{\text{int}} = 0.2$ (see Section 2.3). After repeating this for each redshift step and each map tile (see Section 2.2), we have assembled an oversampled mock catalog containing true masses, redshifts, and mock \tilde{y}_0 values (and their uncertainties) over the full ACT DR5 cluster search area that extends well below the mass selection limit. We then project this catalog onto a $(\log_{10} M_{500c}, z)$ grid and estimate the completeness as the fraction of the mock clusters in each $(\log_{10} M_{500c}, z)$ bin that are above a chosen $S/N_{2.4}$ detection threshold. We repeat this process 1000 times, taking the average as the estimate of the overall survey completeness.

Figure 7 shows the 90% completeness limit as a function of redshift in terms of M_{500c}^{UPP} for $S/N_{2.4} > 5$ over the full 13,211 deg^2 survey area. Evaluated at $z = 0.5$ (approximately the median redshift of the cluster sample; see Section 3), we estimate that the cluster catalog is 90% complete for $M_{500c}^{\text{UPP}} > 3.8 \times 10^{14} M_{\odot}$. The survey is slightly more sensitive to lower mass clusters than that in areas that overlap with the DES, HSC, and KiDS optical surveys ($M_{500c}^{\text{UPP}} > 3.6 \times 10^{14} M_{\odot}$). This statement relates only to the

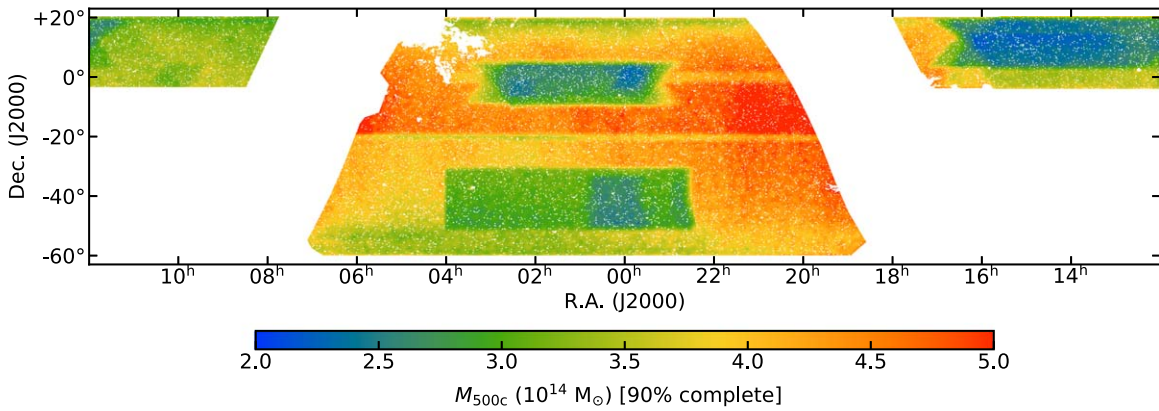


Figure 8. Map of the 90% completeness mass limit for $S/N_{2,4} > 5$ as a function of redshift, in terms of M_{500c}^{UPP} , evaluated at $z = 0.5$ (the median redshift of the detected clusters). The variation is driven by the ACT observing strategy.

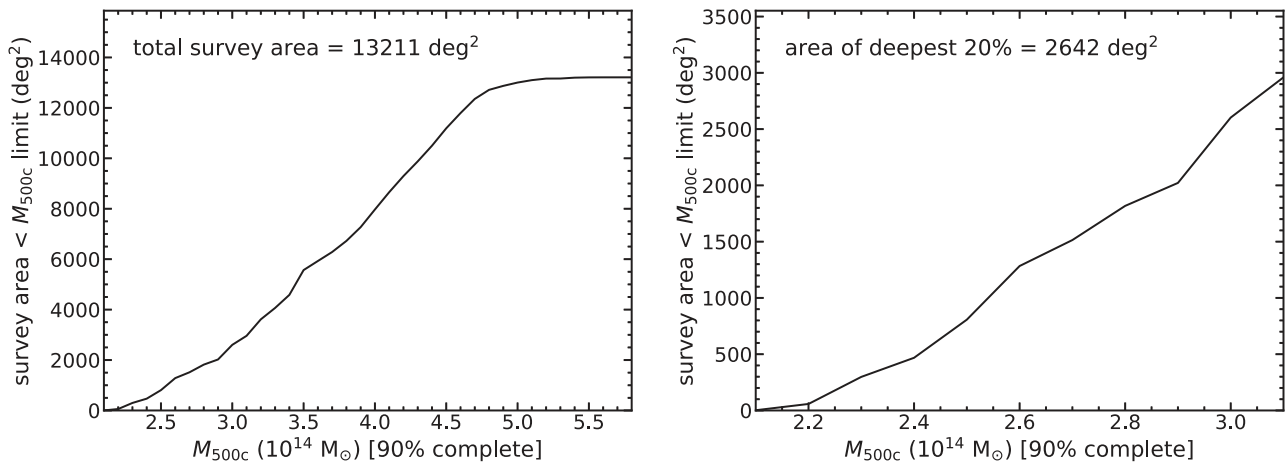


Figure 9. Mass sensitivity in terms of M_{500c}^{UPP} , evaluated at $z = 0.5$, as a cumulative function of area, for the whole survey (left), and for the deepest 20% (right).

noise levels in the ACT maps in the regions of overlap; that is, no optical information is used in deriving estimates of the survey mass limit.

There is a fairly large spatial variation in the mass completeness limit across the map, as shown in Figure 8, which is driven by the ACT observing strategy. Figure 9 shows the cumulative survey area as a function of the estimated mass completeness limit. Almost all of the vastly increased survey area reaches a lower mass limit than previous ACT cluster surveys (Marriage et al. 2011; Hasselfield et al. 2013; Hilton et al. 2018). Clusters with masses in the range $2.1 < M_{500c}^{\text{UPP}}/10^{14} M_{\odot} < 3.1$ can be detected in the deepest 20% of the survey, corresponding to an area of 2634 deg^2 , which is more than double the area searched in Hilton et al. (2018) and larger than the area searched in the SPT-SZ survey (Bleem et al. 2015b; Bocquet et al. 2019).

3. Optical/IR Follow-up and Redshifts

In this section we describe the process of optical/IR confirmation of SZ-detected candidates as clusters of galaxies. The redshifts assigned to objects in the cluster catalog come from a variety of sources, because the ACT DR5 cluster search area is not covered by a single, deep optical/IR survey. We have attempted to obtain as many reliable redshift estimates as possible, given the data available. We provide details on each of the redshift sources in Section 3.1. Section 3.2 summarizes the process of cross-matching the cluster candidate list against external catalogs, visual inspection of the available optical/IR data, and the process

by which we adopted a single redshift measurement for each cluster. We comment on redshift follow-up completeness and the purity of the cluster candidate list in Section 3.3.

3.1. Redshift Sources

3.1.1. Large Public Spectroscopic Surveys

The large ACT DR5 survey area overlaps with several large public spectroscopic surveys. In this work, we made use of 2dFLenS (Blake et al. 2016), OzDES (Childress et al. 2017), Sloan Digital Sky Survey (SDSS) DR16 (Ahumada et al. 2020), and VIPERS (Scodreggio et al. 2018). We cross-matched the cluster candidate list against each of these surveys in turn and estimated cluster redshifts using an iterative procedure similar to that used in Hilton et al. (2018). For each cluster in the list, we first select only galaxies with secure spectroscopic redshifts located within a projected distance of 1 Mpc from the cluster SZ position. We then iteratively estimate the cluster redshift using the biweight location estimator (e.g., Beers et al. 1990), keeping only galaxies with peculiar velocities within 3000 km s^{-1} of the cluster redshift estimated at each iteration. In some iterations, there may be no galaxies found within these peculiar velocity limits (e.g., on rare occasions where the redshift distribution is bimodal). In these cases, we disregard the peculiar velocity cut and take the median of all of the galaxy redshifts as the cluster redshift estimate, before beginning the next iteration. This procedure typically converges within a couple of iterations.

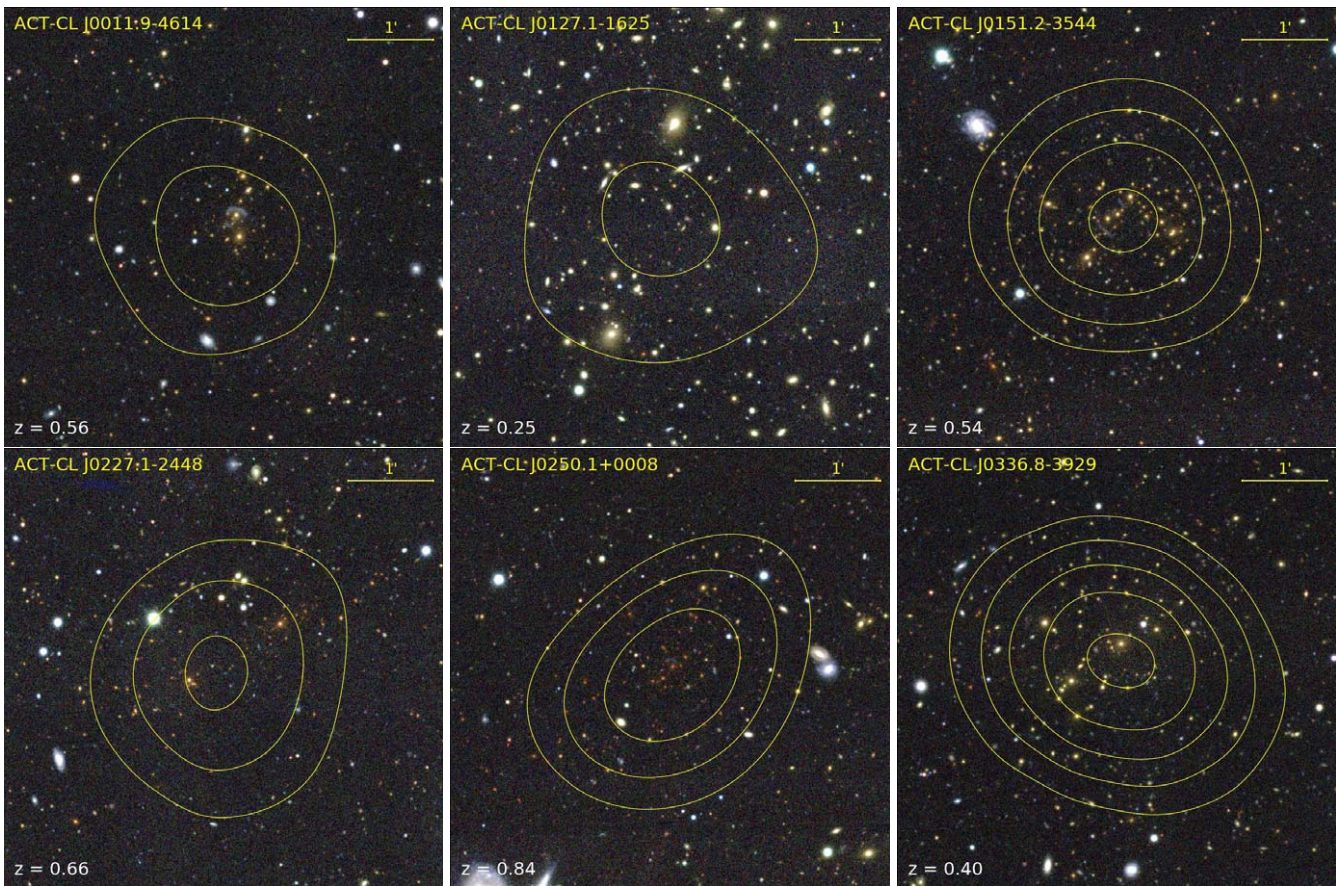


Figure 10. Example DES *gri* images of ACT DR5 clusters at various redshifts confirmed using redMaPPer. Each image is $5'$ on a side, with north at the top and east at the left. The contours mark signal-to-noise ratio in the ACT map filtered at the reference 2.4 scale. The lowest level shown corresponds to 3σ significance, and each subsequent level is 2σ higher.

SDSS DR16 provides the vast majority of spectroscopic redshifts assigned to clusters in the final catalog (1123), followed by 2dFLens (56), OzDES (3), and VIPERS (2). Note that after visual inspection of optical imaging (Section 3.2), we rejected 56 cases of erroneous redshift estimates produced by the above automated procedure in favor of a “manually assigned” spectroscopic redshift (e.g., based on an obvious brightest central galaxy). These objects are flagged in the warnings field of the cluster catalog (see Table 1).

3.1.2. Photometric Redshifts from RedMaPPer

The cluster search area has a large overlap with SDSS (in equatorial regions) and 4566 deg^2 in common with the deep *griz* imaging provided by DES, that is, almost all of the DES footprint (see Figure 1). The DES data used in this work come from the first three years of observations (referred to throughout this paper as “DES Y3”), for which the imaging and photometric catalogs are publicly available as DES DR1¹⁰⁴ (Abbott et al. 2018).

RedMaPPer is an optical red-sequence-based cluster-finding algorithm that was applied to *ugriz* SDSS data (Rykoff et al. 2014) and has subsequently been developed to run on DES photometry (Rykoff et al. 2016). In SDSS, redMaPPer is able to find clusters out to $z \approx 0.5$, while the increased depth of DES allows it to find clusters out to $z \approx 0.9$. One of the key features of redMaPPer is its optical richness measurement (λ), which has been shown to scale with cluster mass (e.g., Simet et al. 2017; McClintock et al. 2019). The photometric redshift estimates

provided by redMaPPer are very accurate, with $\sigma_z/(1+z) < 0.02$ over the full redshift range probed in each survey.

In this work, we use the public SDSS redMaPPer catalog (v6.3; Rykoff et al. 2014) and a new redMaPPer catalog based on the DES Y3 photometry (v6.4.22), containing 33,654 clusters. Both catalogs contain only $\lambda > 20$ systems; at this richness, only 5%–7% of the clusters are expected to be projections along the line of sight (Rykoff et al. 2014, 2016). Since the SZ-selected ACT DR5 cluster catalog may contain clusters at high redshift ($z > 0.8$) that may not be found by redMaPPer alone, we also ran redMaPPer in “scanning mode,” using the prior information of the ACT cluster candidate positions. We found that there is 5% chance association probability of detecting a $\lambda > 20$ system by using redMaPPer in this mode, from a test based on a mock ACT DR5 catalog containing $>93,000$ random positions within the DES Y3 footprint, generated from the \tilde{y}_0 noise map. Note that this represents the average chance association probability; it is possible that this quantity varies with redshift (see the treatment in Klein et al. 2019). Bleem et al. (2020) applied the redMaPPer scanning mode to the SPT Extended Cluster Survey (SPT-ECS) and report a chance association probability similar to that which we find between ACT DR5 and redMaPPer.

We adopted redMaPPer redshifts for 1433 clusters in the ACT DR5 catalog (256 from SDSS, 1023 from DES Y3, and a further 154 from the “scanning mode” run in DES Y3). This is the most from any of the redshift sources used in this work. Figure 10 shows some example images of clusters confirmed using redMaPPer in DES Y3.

¹⁰⁴ <https://des.ncsa.illinois.edu/releases/drl>

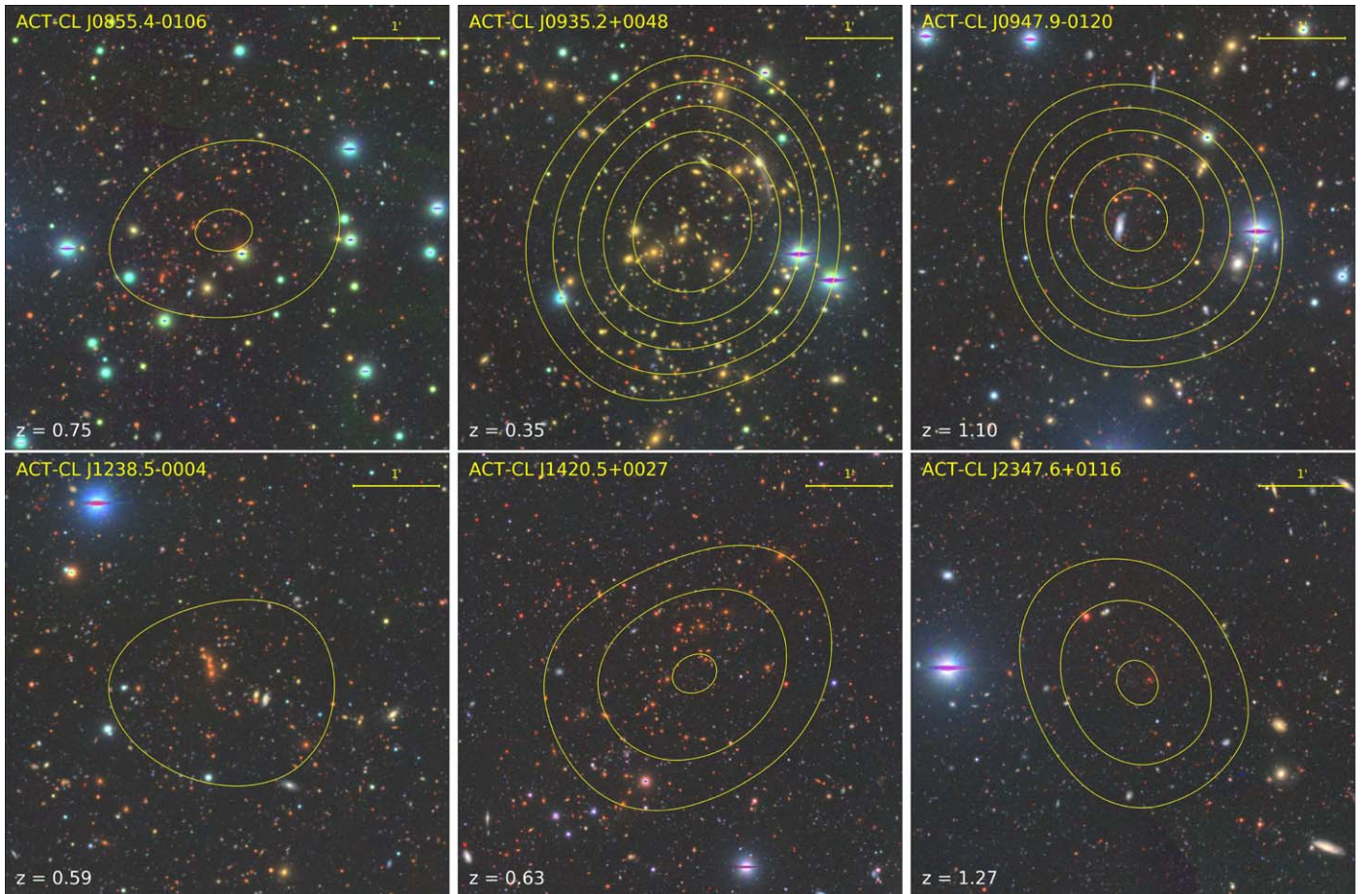


Figure 11. Example *gri* images of ACT DR5 clusters at various redshifts, confirmed using HSC imaging and the CAMIRA optical cluster finder. Each image is 5' on a side, with north at the top and east at the left. The ACT S/N contours have the same scaling as in Figure 10.

3.1.3. Photometric Redshifts from CAMIRA

The Hyper Suprime-Cam Subaru Strategic Program (HSC-SSP) is a deep optical *grizy* survey reaching to depths fainter than 26th magnitude in the *r*-band (Miyazaki et al. 2018; Aihara et al. 2018). The HSC-SSP full-depth full-color (FDFC) footprint corresponding to observations up to the 2019A semester has 469 deg² of overlap with the ACT DR5 cluster search area, as shown in Figure 1.

An optical cluster-finding algorithm named CAMIRA (Cluster finding Algorithm based on Multi-band Identification of Red-sequence gAlaxies; Oguri 2014), which is similar to redMaPPer but was developed independently, has been run on the HSC data. Here we use the CAMIRA cluster catalog based on HSC-SSP S19A photometry; note that the CAMIRA cluster search uses a less conservative mask and covers slightly more area than the FDFC mask. The photometric redshift estimates provided by CAMIRA have low scatter ($\sigma_z/(1+z) = 0.008$ at $z < 1.1$; $\sigma_z/(1+z) \approx 0.02$ for $z > 1.1$) and reach to $z \approx 1.4$ (higher than the $z < 1.1$ limit in the S16A catalog; Oguri et al. 2018). The richness measure used in CAMIRA (N_{mem}) counts the number of red-sequence galaxies in a background-corrected circular aperture, in a manner similar to the λ quantity used in redMaPPer (see Oguri 2014 for a detailed definition). Similarly to redMaPPer, we also ran CAMIRA in “scanning mode,” using prior information of ACT candidate positions. We find that the 5% chance association probability corresponds to a richness threshold of $N_{\text{mem}} > 16$ by running the algorithm on a

catalog of random positions drawn from a mock ACT DR5 cluster catalog. We use this to set the minimum N_{mem} threshold when considering cross-matches against the CAMIRA catalog.

We adopted redshifts for 58 clusters from CAMIRA (only seven of these are from the “scanning mode” run). Figure 11 shows some example clusters confirmed using CAMIRA.

3.1.4. Photometric Redshifts from zCluster

The zCluster algorithm, described in Hilton et al. (2018), estimates redshifts for galaxy clusters using broadband photometry, given a priori knowledge of the cluster position. This is done using a weighted sum of the redshift probability distributions for galaxies along the line of sight to a cluster candidate. In addition to the redshift estimate, zCluster also provides a measure of optical density contrast,

$$\delta(z_c) = \frac{n_{0.5 \text{ Mpc}}(z_c)}{A n_{3-4 \text{ Mpc}}(z_c)} - 1, \quad (7)$$

where z_c is the estimated photometric redshift for the cluster, $n_{0.5 \text{ Mpc}}(z_c)$ is the number of galaxies within 0.5 Mpc projected distance of the given cluster position, $n_{3-4 \text{ Mpc}}(z_c)$ is a measure of the background number of galaxies in a circular annulus 3–4 Mpc from the cluster position, and A is a factor that accounts for the difference in area between these two count measurements. As shown in Hilton et al. (2018), a δ threshold can be used to identify cluster candidates with unreliable redshift estimates.

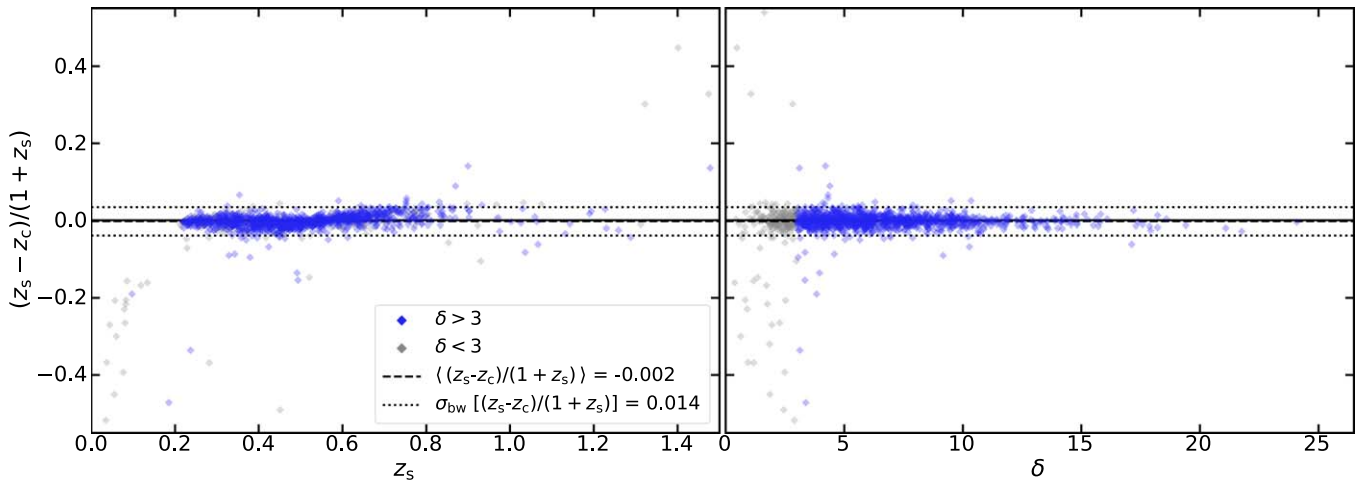


Figure 12. The left panel shows a comparison of spectroscopic redshifts (z_s) with zCluster photometric redshifts (z_c) based on DECaLS DR8 photometry. More than 98% of the objects are recovered within $\Delta z/(1 + z_s) < 0.05$ of the spectroscopic redshift. Note that a bias correction of the form $z = z_c + 0.02(1 + z_c)$ has been applied to the photometric redshifts. The right panel illustrates how the scatter in the photometric redshifts varies with the δ statistic. Objects with $\delta > 3$ are highlighted; many objects with δ below this threshold have accurate redshift estimates, but the scatter is much larger.

In this work, we applied zCluster to photometric data from the Dark Energy Camera Legacy Survey (DECaLS DR8; Dey et al. 2019), the Kilo Degree Survey (KiDS DR4; Wright et al. 2019), and SDSS (DR16; Ahumada et al. 2020). DECaLS provides optical grz photometry combined with 3.4, 4.6 μm photometry from the Wide-field Infrared Survey Explorer mission (WISE; Wright et al. 2010) and covers most of the ACT DR5 cluster search area footprint (10,822 deg^2 of overlap). We find that zCluster is able to measure cluster redshifts out to $z \approx 1.4$ when applied to DECaLS, due to the inclusion of the WISE data. KiDS DR4 provides $ugriZYJHK_s$ photometry over 825 deg^2 in common with ACT DR5, with near-infrared data provided by the VISTA Kilo degree Infrared Galaxy survey (VIKING; Edge et al. 2013).

This work benefits from several improvements that have been made to zCluster, which we briefly summarize here: (1) a new automated masking procedure is used, which constructs an area mask image using the positions of objects in the catalog and the typical nearest-neighbor separation, resulting in more accurate δ estimates close to survey boundaries; (2) bootstrap resampling is used to estimate the uncertainty on the density contrast statistic ($\Delta\delta$) at all points along the redshift range, and redshifts at which $\delta/\Delta\delta < 3$ are rejected; and (3) we have added the ability to easily swap the spectral template set used for the individual galaxy photometric redshift estimates.

While we ran zCluster on SDSS and KiDS photometry using the same set of spectral templates as used in Hilton et al. (2018), that is, the default templates from the EAZY photometric redshift code (Brammer et al. 2008), supplemented by the Coleman et al. (1980, CWW hereafter) templates, we found it necessary to switch the spectral template set in order to optimize the performance when running on DECaLS photometry. We used a subset of the spectral templates used in the COSMOS survey (Ilbert et al. 2009; Salvato et al. 2011), representing a range of normal galaxies and active galactic nuclei (AGNs), removing all elliptical templates based on Bruzual & Charlot (2003) stellar population synthesis models (as these were found to give biased results for individual galaxies at moderate redshifts; we speculate that this is probably related to the extrapolation of the stellar population synthesis models into the WISE bands), and adding in the CWW template set.

Figure 12 presents a comparison between 1168 clusters with spectroscopic redshifts (z_s) and zCluster photometric redshift

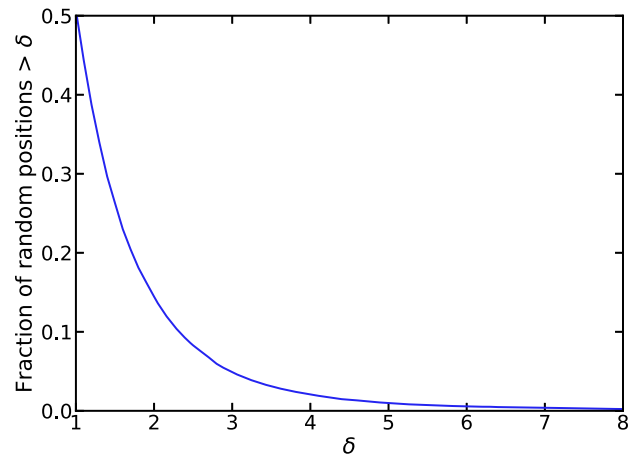


Figure 13. Fraction of random positions drawn from a mock ACT DR5 cluster catalog where δ , the zCluster density contrast statistic as measured using DECaLS photometry, is greater than some value. We find $\delta > 3$ for 5% of the random points.

estimates (z_c), based on DECaLS photometry. Note that we have corrected the zCluster redshifts for a bias of the form $z = z_c + 0.02(1 + z_c)$, where z represents the corrected photometric redshift. We have not identified the source of this bias as yet, but note that this correction is sufficient to ensure that on average the zCluster redshifts reported in this work are not biased. As shown in Figure 12, for clusters with $\delta > 3$, the scatter in the redshift residuals $\Delta z/(1 + z_s)$ is small ($\sigma_{\text{bw}} = 0.014$; estimated using the biweight scale, e.g., Beers et al. 1990). The scatter rises to $\sigma_{\text{bw}} = 0.04$ for the 16 objects beyond $z > 1$. We find that 98% of the redshifts are recovered within $\Delta z/(1 + z_s) < 0.05$ of the spectroscopic redshift, so the number of catastrophic outliers is small.

To estimate the probability of a cluster candidate being associated with a random position on the sky where $\delta > 3$, we ran zCluster on DECaLS photometry on the same mock cluster catalog used for similar tests of redMaPPer and CAMIRA (Sections 3.1.2 and 3.1.3). Figure 13 shows the results of this exercise. We find that 5% of random positions have $\delta > 3$, rising to 14% for $\delta > 2$ and 26% for $\delta > 1.5$. Nevertheless, as shown in the

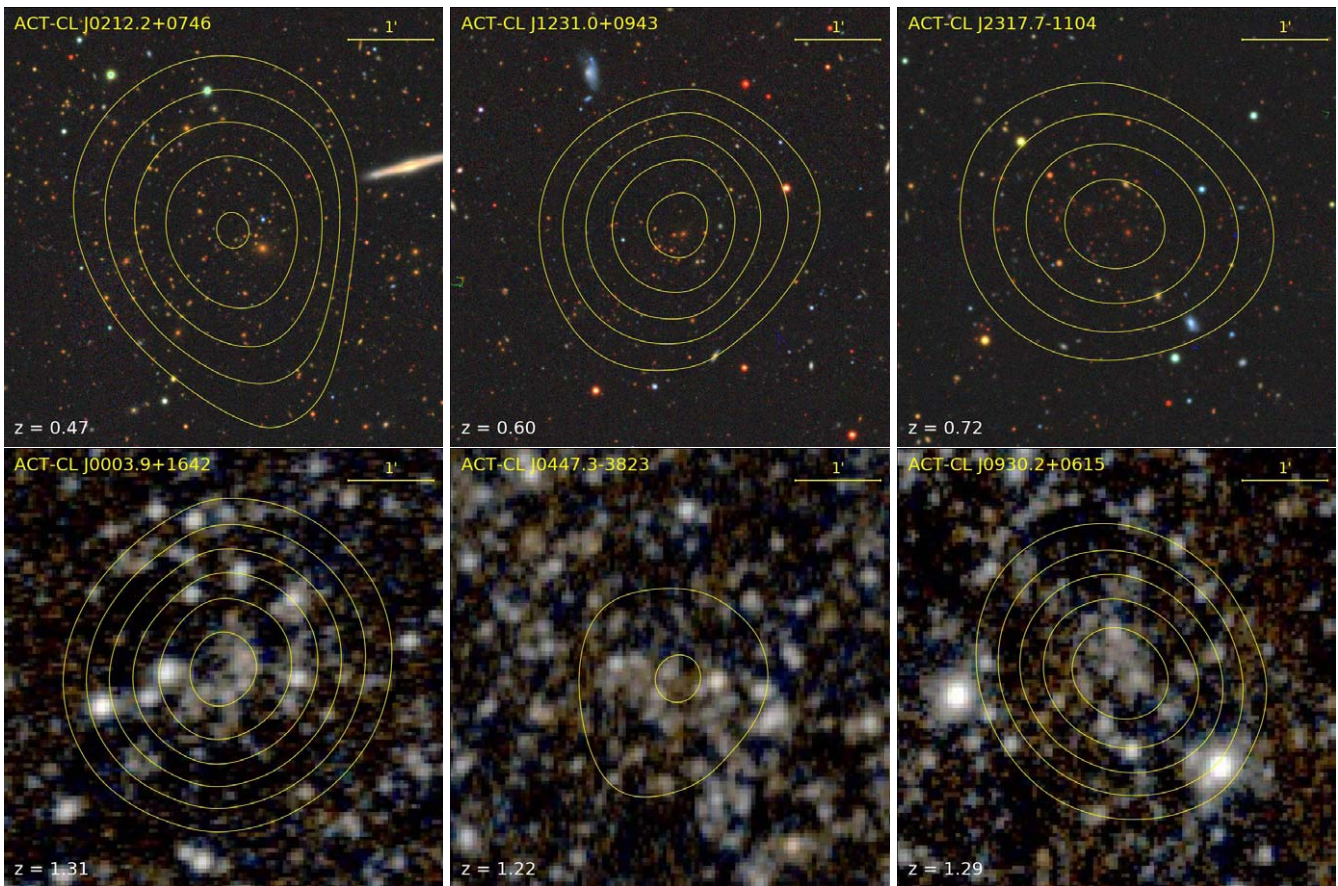


Figure 14. Example DECaLS *grz* images of ACT DR5 clusters at $z < 0.8$ (top row) and unWISE images of $z > 1$ ACT DR5 clusters (bottom row). Each image is $5'$ on a side, with north at the top and east at the left. See Figure 10 for an explanation of the contour levels.

right panel of Figure 12, the zCluster photometric redshift estimates largely remain accurate at $\delta < 3$: we find $\sigma_{\text{bw}} = 0.018$ for objects with $2 < \delta < 3$, with 95% of these objects being found within $\Delta z / (1 + z_s) < 0.05$ of the spectroscopic redshift.

Figure 14 presents images of some example clusters confirmed using zCluster and DECaLS. The ACT DR5 cluster catalog contains 717 objects with redshifts provided by zCluster (706 based on DECaLS photometry, four based on KiDS data, and seven based on SDSS DR16). For 13 of the measurements based on DECaLS, we applied a $z > 0.6$ prior to avoid confusion with projected lower z systems that were judged not to be the source of the SZ signal after visual inspection of the available imaging. In 96 cases where no alternative estimate is available, we adopt zCluster redshifts with $\delta < 3$. All of these exceptions are appropriately flagged in the warnings field of the cluster catalog (see Table 1).

3.1.5. Spectroscopic Redshifts from BEAMS

The BEAMS project (Brightest cluster galaxy Evolution with ACT, MeerKAT, and SALT) is a Large Science Program on the Southern African Large Telescope (SALT) that is obtaining long-slit spectroscopic observations of around 150 cluster central galaxies in a representative sample of $0.3 < z < 0.8$ ACT clusters. BEAMS observations began in 2019 May, and at the time of writing 54 clusters have been observed. The SALT data in hand have been processed with a modified version of the pipeline described in Hilton et al. (2018). In this work, we report spectroscopic redshifts from BEAMS (labeled SALTSpec in

Table 2) for 15 clusters that would otherwise have only photometric estimates.

3.1.6. Other Redshift Sources

We adopted a large number of redshifts used in the ACT DR5 cluster catalog from various sources in the literature. In particular, we used redshifts from previously published SZ surveys by ACT (Menanteau et al. 2013; Sifón et al. 2016; Hilton et al. 2018), Planck (Planck Collaboration et al. 2016b), and SPT (Bleem et al. 2015b, 2020; Bocquet et al. 2019); optically selected cluster catalogs based on SDSS (Wen et al. 2012; Wen & Han 2015, labeled as “WHL” in this work), KiDS DR3 (Maturi et al. 2019, photometric redshifts based on the AMICO cluster-finding algorithm), and ESO ATLAS (B. Ansarinejad et al. 2020, in preparation, photometric redshifts based on the ORCA cluster-finding algorithm; Murphy et al. 2012); and the IR-selected Massive Distant Clusters of WISE survey (MaDCoWS; Gonzalez et al. 2019), which contains more than 2000 high-redshift ($0.7 < z < 1.5$) clusters selected from a survey area that covers most of the extragalactic sky.

We collected a large number of redshifts using the NASA Extragalactic Database (NED¹⁰⁵). We took care to classify such redshifts as spectroscopic or photometric with appropriate uncertainties. References for these miscellaneous sources can be found in the notes for Table 2.

¹⁰⁵ <https://ned.ipac.caltech.edu/>

Table 2
Breakdown of Redshift Sources Used in the ACT DR5 Cluster Catalog

Source	Number	Fraction (%)	Reference(s)
redMaPPer	1433	34.2	Rykoff et al. (2014, 2016)
PublicSpec	1184	28.2	This work, based on data from 2dFLens (Blake et al. 2016), OzDES (Childress et al. 2017), SDSS (Ahumada et al. 2020), and VIPERS (Scodeggio et al. 2018); see Section 3.1.1
zCluster	717	17.1	This work; see Section 3.1.4
WHL	275	6.6	Wen et al. (2012), Wen & Han (2015)
SPT	201	4.8	Bocquet et al. (2019), Bleem et al. (2020)
Lit	164	3.9	See table notes
CAMIRA	58	1.4	Oguri et al. (2018)
ACT	52	1.2	Menanteau et al. (2013), Sifón et al. (2016), Hilton et al. (2018)
ATLAS	51	1.2	B. Ansarnejad et al. (2020 in preparation)
PSZ2	21	0.5	Planck Collaboration et al. (2016b)
SALTSpec	15	0.4	This work; see Section 3.1.5
MaDCoWS	13	0.3	Gonzalez et al. (2019)
AMICO	11	0.3	Maturi et al. (2019)
Total spectroscopic	1649	39.3	...
Total photometric	2546	60.7	...

Note. The labels given in the Source column correspond to those used in the `redshiftSource` column in the FITS table format cluster catalog (see Table 1). See Section 3.2 for a description of how redshifts were assigned to each cluster. Sources for literature redshifts: Abell et al. (1989), Stocke et al. (1991), Struble & Rood (1991), Gioia & Luppino (1994), Dalton et al. (1994), Hughes et al. (1995), Crawford et al. (1995), Shectman et al. (1996), Cappi et al. (1998), Tucker et al. (1998), De Grandi et al. (1999), Struble & Rood (1999), Caccianiga et al. (2000), Schwoppe et al. (2000), Romer et al. (2000), Böhringer et al. (2000), White (2000), Oegerle & Hill (2001), Cruddace et al. (2002), De Propriis et al. (2002), Gladders et al. (2003), Mullis et al. (2003), Valtchanov et al. (2004), Böhringer et al. (2004), Smith et al. (2004), Allen et al. (2004), Zaritsky et al. (2006), Barkhouse et al. (2006), Pimblet et al. (2006), Ebeling et al. (2007), Burenin et al. (2007), Schmidt & Allen (2007), Gilbank et al. (2008), Cavagnolo et al. (2008), Allen et al. (2008), Gal et al. (2009), Coziol et al. (2009), Dawson et al. (2009), Sharon et al. (2010), Wuyts et al. (2010), Mantz et al. (2010), Fassbender et al. (2011), Gralla et al. (2011), Geach et al. (2011), Chon & Böhringer (2012), Planck Collaboration et al. (2012), Song et al. (2012), Mann & Ebeling (2012), Mehrrens et al. (2012), Willis et al. (2013), Nastasi et al. (2014), Crawford et al. (2014), Bradley et al. (2014), Lauer et al. (2014), Stanford et al. (2014), Planck Collaboration et al. (2015), Gonzalez et al. (2015), Bleem et al. (2015a), Ehlert et al. (2015), Buddendiek et al. (2015), Proust et al. (2015), Connor et al. (2019).

3.2. Cluster Confirmation and Redshift Assignment

We confirmed SZ-detected candidates as galaxy clusters using the wide variety of surveys described in Section 3.1, in combination with an extensive effort to visually inspect the available optical/IR imaging for a large fraction of the catalog.

To reduce the required visual classification effort, we cross-matched the cluster candidate list against several external cluster catalogs that we deem to be reliable. The cross-matching procedure makes use of the position recovery model given in Equation (3) and shown in Figure 4. We adopt the fit parameters that describe the radial distance as a function of $S/N_{2.4}$ within which 99.7% of the injected clusters were recovered. This accounts for uncertainty in the ACT cluster positions, due to noise fluctuations in the filtered maps. However, the model does not account for position uncertainties in the external cluster catalogs. Therefore, we add in quadrature the equivalent of an additional 0.5 Mpc projected distance to the cross-matching radius, evaluated at the redshift reported in the catalog being cross-matched. This serves as a conservative estimate of positional uncertainties in the external cross-match catalogs.

We adopt a single redshift for each cluster in the catalog, after consideration of the various potential redshift measurements available. Table 2 lists the number of redshifts used from each potential source together with the appropriate references. Where possible, first preference is given to a spectroscopic redshift. If this is not available, for clusters that have cross-matches against external cluster catalogs, we select a photometric redshift according to the following in order of preference: (1) redMaPPer in DES Y3, (2) CAMIRA, (3) SPT, (4) redMaPPer in SDSS, (5) WHL. The order reflects the fact that we give preference to redshifts measured in deeper optical surveys.

We assigned redshifts from AMICO, ESO ATLAS, MaDCoWS, PSZ2, zCluster, and miscellaneous literature sources (labeled Lit in Table 2) to clusters after visual inspection of the optical/IR imaging from DECaLS, DES, KiDS, SDSS, HSC-SSP, Pan-STARRS (PS1; Flewelling et al. 2016), and WISE. We similarly visually inspected all objects with redshifts derived from public spectroscopic surveys to check that the redshift assignment was sensible (i.e., derived from cluster member galaxies such as the BCG). Note, however, that although the catalog contains clusters detected with $S/N > 4$, visual inspection of cluster candidates is only complete for all objects with $S/N_{2.4} > 5$. Objects with $S/N_{2.4} < 5$ have only been visually inspected if there is some evidence from an external source that they may be galaxy clusters (e.g., $\delta > 3$ as measured by zCluster, or a cross-match with an optical/IR-selected cluster catalog).

3.3. Purity and Follow-up Completeness

The fraction of optically confirmed cluster candidates above a given signal-to-noise threshold can be used to assess the purity of a cluster sample, in the case of a complete set of follow-up observations (e.g., Menanteau et al. 2010). Currently, we do not have all of the deep optical and IR data that would be needed to determine the nature of all of the sources in the ACT DR5 cluster candidate list in the full 13,211 deg² survey area. Due to the redshift-independent nature of the SZ effect, it is possible for candidates to be located at distances that place them beyond the reach of our available imaging. Therefore, in the high-S/N regime, where the cluster sample is expected to be highly pure (see Figure 6), the fraction of optically confirmed clusters in the ACT DR5 sample gives an indication of the completeness of follow-up. At low S/N, this measure is instead driven by the false-positive detection rate.

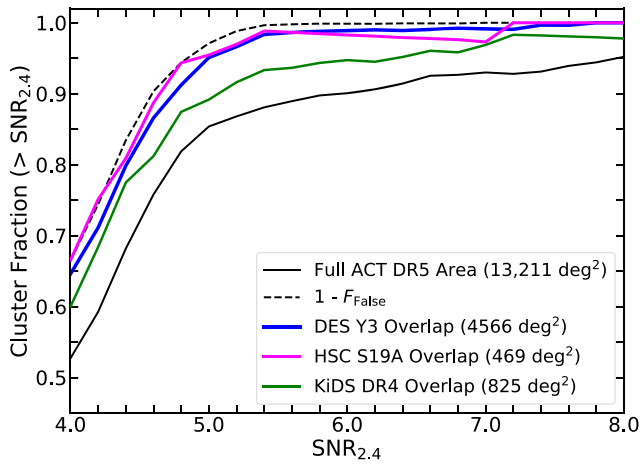


Figure 15. Fraction of ACT DR5 cluster candidates that are optically confirmed as clusters (with a redshift measurement) as a function of $S/N_{2.4}$, broken down according to the cluster sample, based on a simulation of the survey (see Section 2.2 and Figure 6). The dashed line (labeled $1 - F_{\text{False}}$) shows the expected purity of the cluster sample, based on a simulation of the survey (see Section 2.2 and Figure 6). The small difference between $1 - F_{\text{False}}$ and the tracks for the DES Y3 and HSC regions indicates that the optical follow-up is essentially complete for these parts of the sky. However, the difference between $1 - F_{\text{False}}$ and the full ACT DR5 survey footprint indicates the potential for further follow-up to add up to 960 clusters to the sample.

Figure 15 shows the fraction of confirmed clusters as a function of $S/N_{2.4}$ detection threshold, broken down in terms of overlap with deep optical surveys. More than 98% of the ACT DR5 candidates with $S/N_{2.4} > 5.5$ in the regions with DES Y3 or HSC S19A optical coverage are confirmed as clusters and have redshift measurements. The fraction of confirmed clusters above the same $S/N_{2.4}$ cut is slightly lower in the region covered by KiDS DR4 (94%), and significantly lower when the full 13,211 deg^2 ACT DR5 cluster search area is considered (89%). This reflects the fact that a significant fraction of the full ACT DR5 footprint does not have complete coverage with data of similar quality to these deep optical surveys.

As shown in Section 2.2 and Figure 6, we expect 34% of candidates to be false positives for a selection cut of $S/N_{2.4} > 4$, based on a signal-free simulation of the survey. We use this to predict the purity of the sample (labeled as $1 - F_{\text{False}}$ in Figure 15), although as noted earlier, this represents a best-case scenario as the simulations used do not fully capture all of the noise sources present in the real data. We see that this traces the fraction of candidates confirmed as clusters in the DES and HSC regions reasonably well, indicating that further optical follow-up efforts in these areas should produce only a modest increase in the fraction of confirmed clusters. On the other hand, only 52% of 7407 candidates with $S/N_{2.4} > 4$ detected in the full 13,211 deg^2 ACT DR5 footprint are currently optically confirmed, compared to the 66% expected if the estimate of the false-positive rate is accurate. Therefore, further follow-up over the full ACT DR5 area has the potential to add approximately 960 clusters to the sample.

4. The ACT DR5 Cluster Catalog

4.1. Properties of the Cluster Catalog

This release of the ACT cluster catalog consists of 4195 optically confirmed galaxy clusters detected with $S/N > 4$ using the combination of the 98 and 150 GHz ACT maps. Table 1

describes the data provided in the catalog. Each cluster in the catalog has a redshift measurement (see Section 3.1) and a set of mass estimates inferred from our SZ observable, \tilde{y}_0 (see Section 2.3). The left panel of Figure 16 summarizes the contents of the catalog by showing the distribution of the clusters in terms of comoving coordinates in the celestial equatorial plane (i.e., R. A. is used as the angular coordinate). The right panel of Figure 16 shows a similar plot but in spherical polar coordinates.

Several studies have found evidence that cluster masses calibrated against the Arnaud et al. (2010) scaling relation, our fiducial mass estimate (labeled M_{500c}^{UPP} in this work), are lower than those measured from weak lensing (e.g., von der Linden et al. 2014; Hoekstra et al. 2015; Battaglia et al. 2016; Miyatake et al. 2019). For this reason, we provide a set of mass estimates that have been rescaled according to a richness-based weak-lensing mass calibration, following a procedure similar to that described in Hilton et al. (2018).

Using the sample of 383 $S/N_{2.4} > 6$ clusters (expected to be $>98\%$ pure; see Section 3.3) with λ measurements from redMaPPer in the DES Y3 footprint and the McClintock et al. (2019) λ -mass relation, we find that the ratio of the average A10-calibrated SZ mass to the average richness-based, weak-lensing calibrated mass is $\langle M_{500c}^{\text{UPP}} \rangle / \langle M_{500c}^{\text{WL}} \rangle = 0.71 \pm 0.07$. Masses that have been rescaled according to this calibration factor are labeled M_{500c}^{Cal} throughout this work and for convenience are provided in the cluster catalog (see Table 1). This calibration factor is in good agreement with the value reported in Hilton et al. (2018), which used SDSS redMaPPer λ measurements and the Simet et al. (2017) λ -mass relation. However, if we use the redMaPPer SDSS λ measurements and the Simet et al. (2017) relation (instead of the McClintock et al. 2019 relation) with the ACT DR5 M_{500c}^{UPP} estimates, then we find $\langle M_{500c}^{\text{UPP}} \rangle / \langle M_{500c}^{\text{WL}} \rangle = 0.66 \pm 0.08$.

We present the redshift distribution of the cluster sample in Figure 17. The sample has median $z = 0.52$, similar to other SZ-selected samples (e.g., Hilton et al. 2018; Bocquet et al. 2019; Bleem et al. 2020) and covers the redshift range $0.04 < z < 1.91$. Largely due to the overlap with SDSS, a significant fraction of the redshifts are spectroscopic (39.3%). The highest redshift cluster in the sample, ACT-CL J0217.7-0345, is detected with $S/N_{2.4} = 5.7$ and was first reported as the $z = 1.91^{+0.19}_{-0.21}$ X-ray-selected cluster XLSSU J021744.1-034536 by Willis et al. (2013). It is also the highest redshift SZ-detected cluster currently known (Mantz et al. 2014, 2018). The catalog contains 222 $z > 1$ clusters, which is greater than the total number of clusters reported in the previous ACT cluster catalog (Hilton et al. 2018). Most of the clusters in the catalog have previously been detected in other surveys; here we report 868 new cluster discoveries, with median $z = 0.75$. This figure excludes clusters detected in the redMaPPer DES Y3 and CAMIRA S19A catalogs.

Figure 18 shows the ACT DR5 sample in the (mass, redshift) plane, in comparison with other SZ-selected cluster samples from Planck (Planck Collaboration et al. 2016b) and SPT (Bocquet et al. 2019; Bleem et al. 2020; Huang et al. 2020a). Here we show the richness-based weak-lensing calibrated masses from ACT (M_{500c}^{Cal}), as these are on a mass scale similar to SPT (see Section 5.1). We plot both the full ACT DR5 sample down to $S/N > 4$ (shown as the small blue points) and a subsample with a cut of $S/N_{2.4} > 5$ applied, which is closer to the detection thresholds used in the other surveys and more closely resembles the sample that will be used for future cosmological analyses. The ACT DR5 sample contains more clusters than all of the previous blind SZ cluster searches

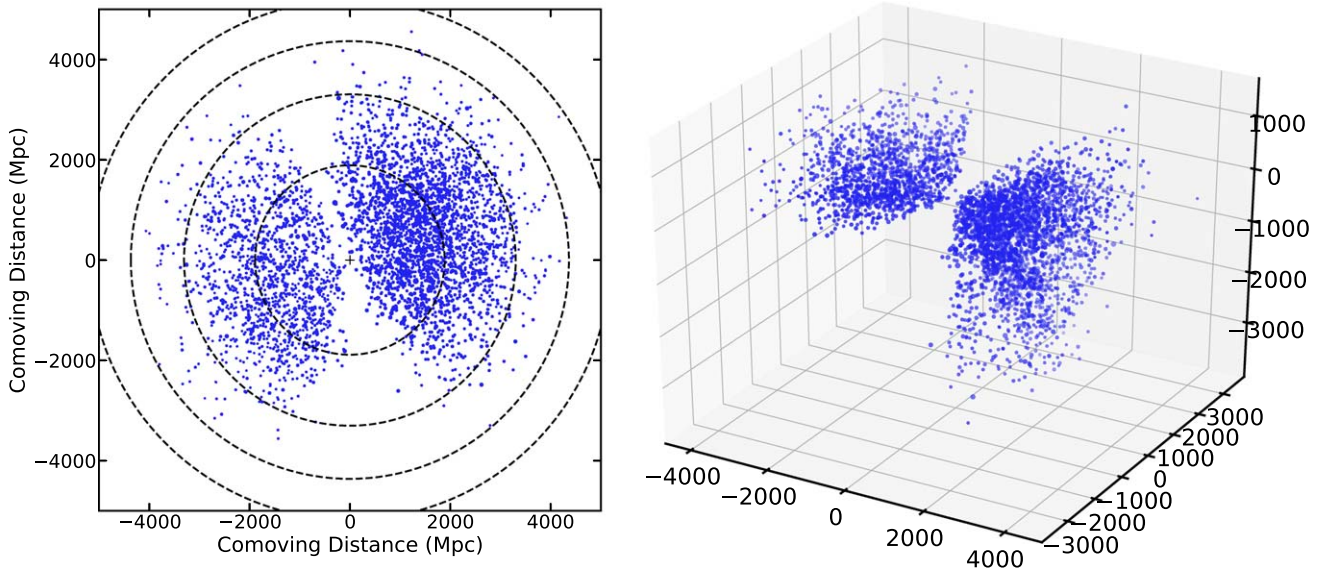


Figure 16. The left panel displays a wedge plot showing the contents of the ACT DR5 cluster catalog, drawn in the equatorial plane. R.A. is used as the angular coordinate, with 0° R.A. pointing to the right from the origin and increasing counterclockwise. The radial coordinate is comoving distance in Mpc. Each point represents a cluster in the catalog, with the size of each point scaling with cluster mass. The dashed circles mark the distances equivalent to redshifts 0.5, 1.0, 1.5, and 2.0, starting from the observer’s location at (0, 0). The larger number of clusters seen on the right of the plot compared to the left reflects the fact that ACT surveyed much more sky area at those R.A. coordinates (see Figure 1). The right panel shows a 3D projection of the same information in spherical polar coordinates; here the axes are comoving distance in Mpc.

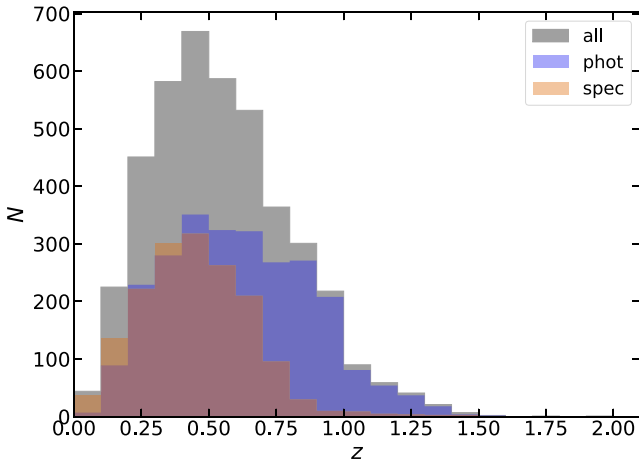


Figure 17. Redshift distribution of the ACT DR5 cluster sample. The sample spans the redshift range $0.04 < z < 1.91$ (median $z = 0.52$). The distribution split according to redshift type (spectroscopic or photometric) is also shown; 39.3% of the clusters in the sample have spectroscopic redshifts.

combined. Due to the higher spatial resolution of the instruments, both the ACT DR5 and SPT samples reach to significantly lower mass limits than the PSZ2 catalog for $z > 0.2$. As Figure 18 shows, the SPTpol sample (Huang et al. 2020a) is more sensitive to lower mass clusters than ACT DR5 when a similar detection threshold is applied, although this survey covers only 94 deg^2 .

Inspection of Figure 18 suggests that there may be a deficit of clusters in the redshift range $1 < z < 1.1$. This is extremely unlikely to be a real feature and may arise from a bias in the photometric redshifts. We will investigate this further with future spectroscopic follow-up of such high-redshift systems.

4.2. Comparison with the ACT DR3 Cluster Catalog

As discussed extensively in Choi et al. (2020) and Aiola et al. (2020), there have been many changes to the ACT data

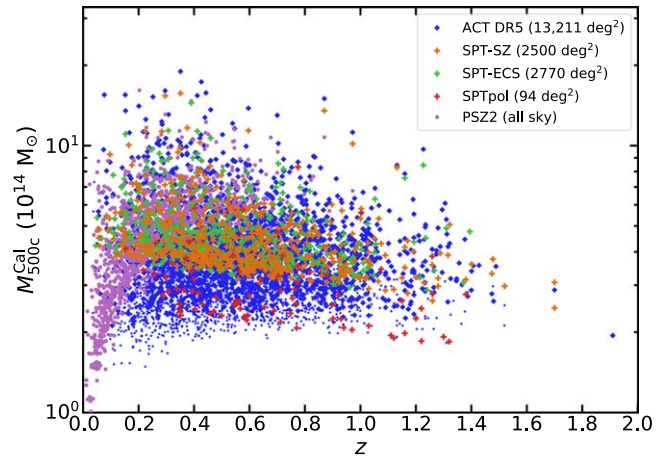


Figure 18. Comparison of the ACT DR5 cluster sample in the (mass, redshift) plane with other blind SZ surveys: PSZ2 (Planck Collaboration et al. 2016b), SPT-SZ (Bocquet et al. 2019), SPT-ECS (Bleem et al. 2020), and SPTpol (Huang et al. 2020a). The large blue points show the ACT DR5 sample selected with $S/N_{2.4} > 5$, which is similar to the detection thresholds used in the other surveys. The small blue points extend this to include the full ACT DR5 sample. The ACT DR5 SZ masses displayed here have been rescaled according to a richness-based weak-lensing mass calibration, which is a close match to the SPT mass scale (see Section 5.1). Mass measurements from the SPT surveys and PSZ2 are as reported in the respective catalogs. The ACT DR5 sample has been plotted behind the other surveys to aid clarity.

processing pipelines at all levels of the analysis since the data release that the Hilton et al. (2018) ACTPol cluster catalog (ACT DR3 hereafter) is based on. In this work, we have used maps produced using a new coadding procedure that incorporates data from all observing seasons and, for the first time, includes data taken during the daytime (N20). As noted in Section 2.1, these coadded maps include preliminary data from the 2017 and 2018 observing seasons that have not been subjected to the full battery of tests as used in the CMB power spectrum analysis presented in Choi et al. (2020) and Aiola et al. (2020). In this work, we also use a different,

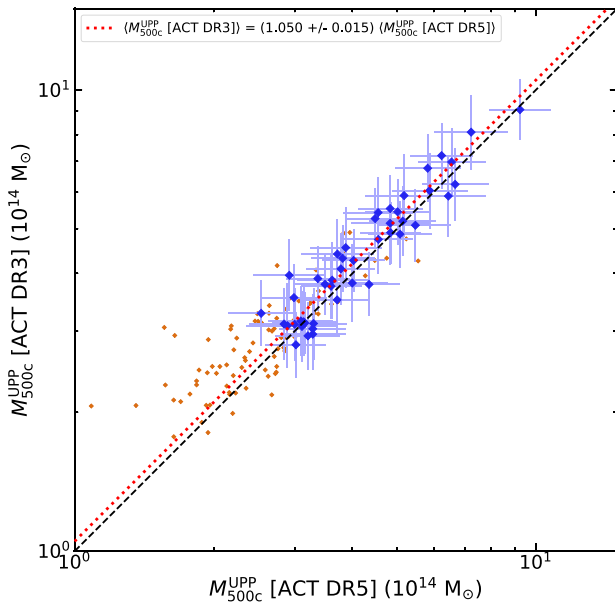


Figure 19. Comparison between ACT DR5 mass estimates (this work, plotted along the horizontal axis) and previous ACT cluster mass estimates as reported in Hilton et al. (2018, labeled ACT DR3). Both analyses assume the same scaling relation between SZ signal and mass. The large blue points are objects with $S/N_{2.4} > 6$ in both samples (for which the unweighted mean ratio is calculated, shown by the dotted red line), while the small orange points (without error bars) show objects below this threshold. The dashed black line shows the 1:1 correlation.

multifrequency matched filter approach in the cluster finder compared to the algorithm described in Hilton et al. (2018).

We begin by checking the recovery of ACT DR3 clusters in the ACT DR5 catalog. Hilton et al. (2018) reported the detection of 182 $S/N > 4$ clusters, of which 175/182 are within the ACT DR5 cluster search area (i.e., seven clusters fall within regions masked in DR5). Of these, 154/175 are recovered within $2/5$ of the position of a candidate in the ACT DR5 catalog, leaving 21 clusters that are not detected at $S/N > 4$. The missing 21 clusters have median $S/N = 4.3$ in the ACT DR3 catalog, although three $S/N > 5$ clusters (ACT-CL J0238.2+0245, ACT-CL J0341.9+0105, and ACT-CL J2337.6-0856) are not detected in the ACT DR5 catalog. Half of the missing 21 clusters were previously reported in other catalogs (Goto et al. 2002; Lopes et al. 2004; Durret et al. 2011; Menanteau et al. 2013; Rykoff et al. 2014; Wen & Han 2015). Rerunning the ACT DR5 cluster search with a lower detection threshold recovers 13/21 of the missing ACT DR3 clusters at $S/N > 3$.

Figure 19 presents a comparison of the ACT DR3 mass estimates reported in Hilton et al. (2018) with the new measurements from ACT DR5. We highlight the objects detected with $S/N_{2.4} > 6$ in both samples, as these should not be affected by filter noise bias at any significant level. As expected, both sets of measurements follow a tight correlation. However, we see that the ACT DR5 masses are on average systematically $\approx 7\%$ lower than the ACT DR3 measurements. We have verified that the difference in the filtering approach between Hilton et al. (2018) and this work is not the cause (consistent \bar{y}_0 measurements are obtained when running either method on the same map). It may be the case that scale-dependent bandpass effects (see Madhavacheril et al. 2020), which are not accounted for in this analysis, could explain part of the offset. While we have not yet been able to resolve this

discrepancy, we note that gain errors at the level of a few percent are expected in the coadded maps analyzed in this work (N20). Therefore, we caution users of the ACT DR5 cluster catalog that the \bar{y}_0 measurements reported here (and in turn the M_{500c}^{UPP} masses) may be systematically underestimated by $\approx 5\%$ – 10% , if the ACT DR3 catalog is taken as “truth.” This should be kept in mind when comparing these values against external catalogs. However, mass calibration against external data sets can still be used to absorb any systematic calibration error (as should be the case for the M_{500c}^{Cal} mass estimates).

5. Discussion

5.1. The SZ Cluster Mass Scale

Mass calibration of cluster samples is the key systematic that limits their ability to constrain cosmological parameters and is a topic of much debate in the literature (e.g., von der Linden et al. 2014; Hoekstra et al. 2015; Battaglia et al. 2016; Planck Collaboration et al. 2016a; Smith et al. 2016; Medezinski et al. 2018; Miyatake et al. 2019). Cluster mass estimation based on any kind of data is dependent upon a number of assumptions. Here we present a simple comparison of the mass estimates available in the ACT DR5 catalog with previous SZ surveys, and a compendium of weak-lensing mass estimates (CoMaLit; Sereno 2015), as an illustration of how they may be used. Future works based on the ACT DR5 catalog will investigate this topic in much more detail.

In Hilton et al. (2018), we presented comparisons between ACT cluster mass estimates and the SPT-SZ and PSZ2 catalogs. While we found excellent agreement with the Bleem et al. (2015b) SPT-SZ catalog, we noted an apparent mass-dependent trend when comparing the ACT masses with PSZ2 (although at low significance). This was identified in a plot of the ACT-PSZ2 mass ratio versus the ACT mass estimate. We subsequently found that the apparent mass-dependent trend was an illusion driven by the combination of a regrettable choice in the plot axes (i.e., plotting the ACT mass instead of the PSZ2 mass as the independent coordinate), the very different selection of the ACT and PSZ2 cluster samples (PSZ2 detects $z < 0.2$ clusters at high significance down to low masses while ACT does not, and the reverse is true at higher z), and that the measurements themselves are subject to a significant amount of scatter, especially at low signal-to-noise ratio. We rectify this in the comparisons presented here by simply plotting the mass estimates in each catalog against each other.

Figure 20 shows a comparison between the ACT DR5 masses rescaled using the richness-based weak-lensing mass calibration (see Section 4) against a union of the SPT cluster catalogs (Bocquet et al. 2019; Bleem et al. 2020; Huang et al. 2020a; note that we make no attempt to remove duplicate objects). This “SPT-Union” sample contains 618 clusters in common with ACT DR5 (326 from SPT-SZ, 266 from SPT-ECS, and 26 from SPTpol) if we include all objects down to the detection thresholds used by each survey. The masses are clearly correlated, although there is a tendency for the ACT mass estimates to be slightly larger than those from SPT, particularly at the high mass end.

Leaving aside any question of mass-dependent scaling for future work, we can make a simple assessment of the overall consistency of the mass scale between the two samples using the unweighted mean ratio of their masses (e.g., Sifón et al. 2016; Hilton et al. 2018). Here we use the 254 objects

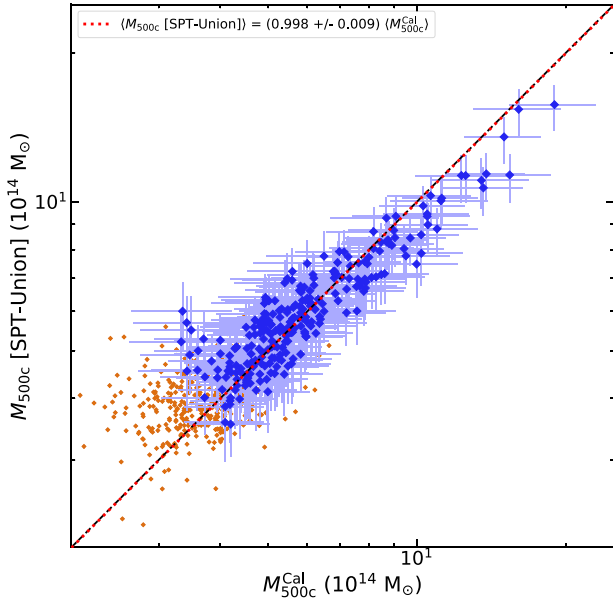


Figure 20. Comparison between ACT DR5 mass estimates rescaled according to a richness-based weak-lensing mass calibration (M_{500c}^{Cal} ; Section 4) with SPT masses reported in Bocquet et al. (2019), Bleem et al. (2020), and Huang et al. (2020a). The large blue points are objects with $S/N > 6$ in both ACT and SPT (for which the unweighted mean ratio is calculated, shown by the dotted red line), while the small orange points (without error bars) show objects below this threshold. The dashed black line shows the 1:1 correlation.

detected at $S/N > 6$ in both samples, as $>98\%$ of the ACT DR5 candidates with $S/N_{2.4} > 6$ were confirmed to be clusters in the DES Y3 and HSC S19A regions (see Section 3.3). Using a high S/N threshold also mitigates the effect of the “noise floor” in the case of a significant difference in depth between two samples (although that is not the case for the comparison here). We find $\langle M_{500c} [\text{SPT-Union}] \rangle = (0.998 \pm 0.009) \langle M_{500c}^{\text{Cal}} \rangle$, where the uncertainty is the standard error on the mean (note that this does not account for the uncertainty on the richness-based weak-lensing mass calibration factor itself). We find results that are consistent with this if we compare ACT DR5 against the individual SPT catalogs: $\langle M_{500c} [\text{SPT-SZ}] \rangle = (1.027 \pm 0.012) \langle M_{500c}^{\text{Cal}} \rangle$; $\langle M_{500c} [\text{SPT-ECS}] \rangle = (0.961 \pm 0.014) \langle M_{500c}^{\text{Cal}} \rangle$; and $\langle M_{500c} [\text{SPTpol}] \rangle = (1.001 \pm 0.027) \langle M_{500c}^{\text{Cal}} \rangle$. Similarly to Hilton et al. (2018), we see that despite the differences between how the ACT DR5 and SPT samples were constructed, and the very different method used to calibrate the mass estimates, the richness-based weak-lensing calibrated masses are on a mass scale similar to SPT.

Figure 21 presents a similar comparison between ACT DR5 and the PSZ2 catalog (Planck Collaboration et al. 2016b). Since we adopted the same fiducial X-ray-calibrated mass-scaling relation from A10 as used in the PSZ2 catalog, we would expect the ACT DR5 clusters to follow the same mass scale. Here the comparison is made against ACT DR5 mass estimates that neglect the bias correction that accounts for the steepness of the cluster mass function, as such a correction is not applied to the masses reported in the PSZ2 catalog (see Section 2.3 and the discussion in Battaglia et al. 2016). We use a $5'$ radius to cross-match the two catalogs, resulting in a sample of 327 clusters, if we include all objects down to the detection threshold of each survey. As shown in Figure 21, the scatter between the PSZ2 and ACT DR5 masses is large, but

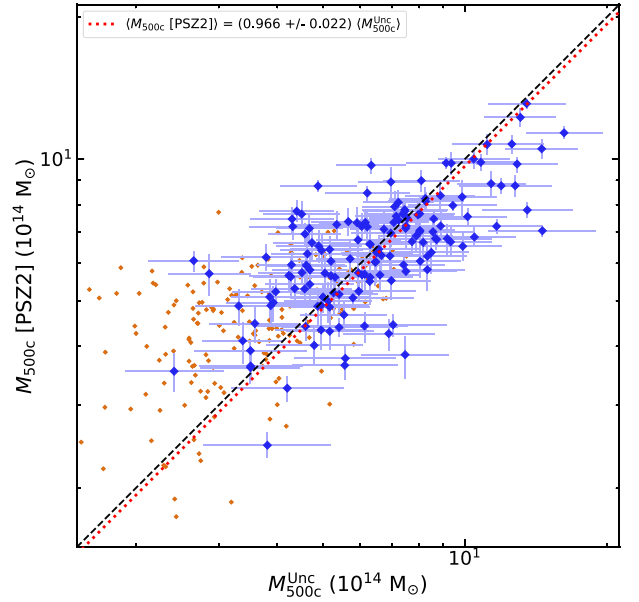


Figure 21. Comparison between ACT DR5 mass estimates, uncorrected for bias due to the steepness of the cluster mass function (M_{500c}^{Unc} ; Section 4), with PSZ2 masses reported in Planck Collaboration et al. (2016b). The large blue points highlight objects with $S/N > 6$ in both surveys, while the small orange points (without error bars) show objects below this threshold. The lines have the same meaning as in Figure 20.

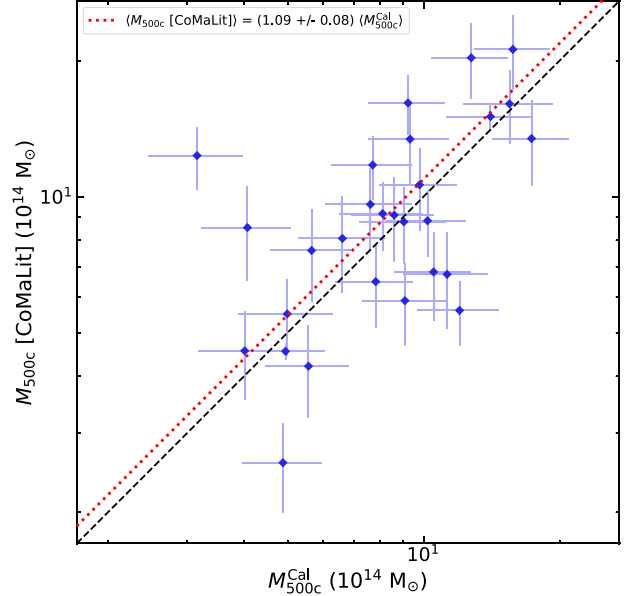


Figure 22. Comparison between ACT DR5 mass estimates rescaled according to a richness-based weak-lensing mass calibration (M_{500c}^{Cal} ; Section 4) with weak-lensing masses from the CoMaLit database (Sereno 2015). Here we use the LC^2 -single catalog from CoMaLit, which consists of objects modeled using a single halo, and we restrict the selection to include only clusters with weak-lensing mass estimates with $<25\%$ uncertainties. The lines have the same meaning as in Figure 20.

the mass scale is indeed similar: we find $\langle M_{500c} [\text{PSZ2}] \rangle = (0.966 \pm 0.022) \langle M_{500c}^{\text{Unc}} \rangle$ from the 148 objects detected with $S/N > 6$ in both catalogs.

As an independent check of the richness-based weak-lensing mass calibration used in this work, Figure 22 presents a comparison with a heterogeneous database of weak-lensing

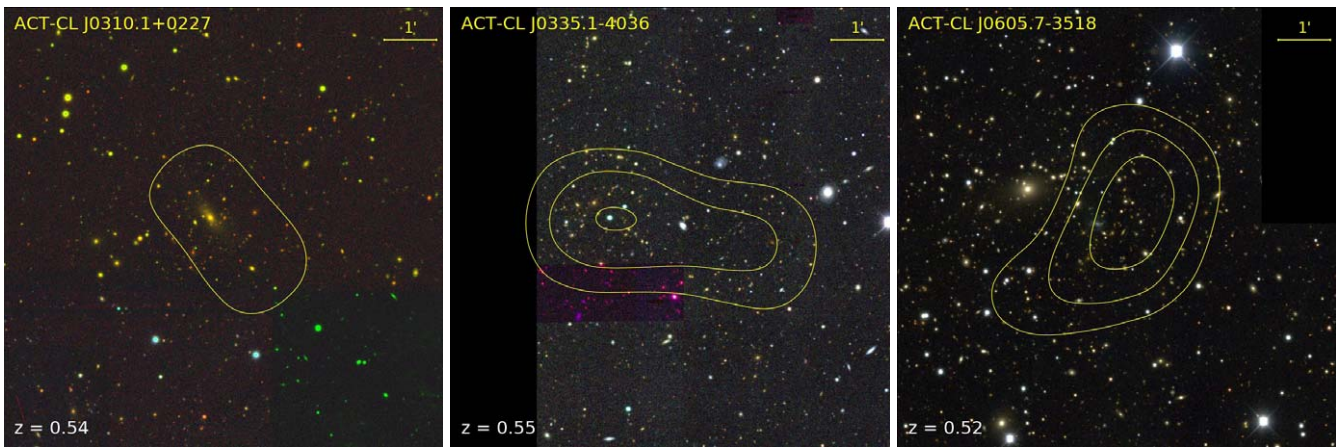


Figure 23. Examples of possible projected systems (see Section 5.2.1). Each image is $8'$ on a side, with north at the top and east at the left. See Figure 10 for an explanation of the contour levels.

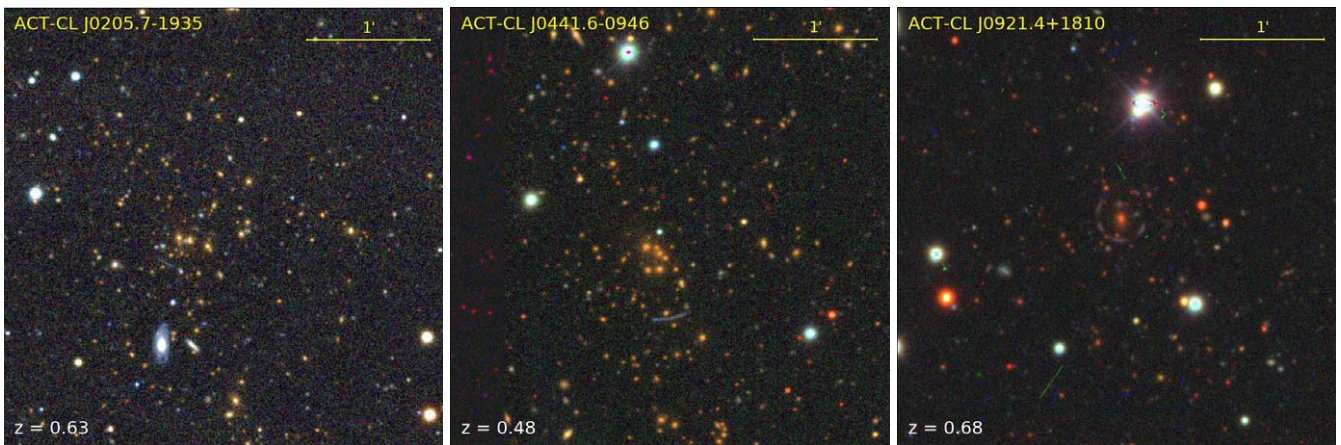


Figure 24. Examples of systems that show possible strong gravitational lensing features (see Section 5.2.2). ACT-CL J0205.7-1935 contains a lens candidate in the H. T. Diehl et al. (2020, in preparation) catalog; ACT-CL J0441.6-0946 contains the known lens DESI-070.4130-09.7774 (Huang et al. 2020c); and the lens in ACT-CL J0921.4+1810 appears to be identified for the first time in this work. Each image is $3.5'$ on a side, with north at the top and east at the left.

masses assembled from the literature (Serenio 2015). Even though the comparison is made only with clusters that have $<25\%$ uncertainty in the weak-lensing masses, the scatter is large. Nevertheless, the overall mass scale is consistent with the richness-based weak-lensing calibration derived from DES observations: $\langle M_{500c}[\text{CoMaLit}] \rangle = (1.09 \pm 0.08) \langle M_{500c}^{\text{Cal}} \rangle$. Future work will explore the mass calibration of the ACT DR5 sample using optical weak-lensing data from DES, HSC-SSP, and KiDS, as well as from gravitational lensing of the CMB.

5.2. Notable Clusters

In this section we briefly discuss a few notable categories of systems that may be of interest for future studies. This list is not meant to be comprehensive, and results for the most part are from visual inspection of the cluster catalog using the available optical/IR data (see Section 3.2). Further possible examples besides those mentioned here may be found by inspecting the `notes` and `warnings` columns of the cluster catalog (see Table 1).

5.2.1. Projected Systems

During visual inspection of the cluster candidates, we identified 46 systems that may be projections of two or more clusters at different redshifts. These are indicated in the `warnings` field of

the cluster catalog (see Table 1). Figure 23 shows a few examples. One of these cases (ACT-CL J0335.1-4036) is clearly a blended SZ detection of two systems, which the cluster finder has failed to separate because all of the pixels in both systems are well above our detection threshold. We will seek to improve the object deblending for future cluster catalog releases.

5.2.2. Strong Lensing Systems

A search of the literature shows that there are 210 known strong gravitational lenses located within 2 Mpc projected distance of clusters in the ACT DR5 release, as recorded in the `knownLens` field of the cluster catalog (see Table 1). Table 3 lists the lens catalogs that were searched and the corresponding code used in the `knownLensRefCode` in the cluster catalog. We also identified a further 67 clusters that show possible strong lensing features, based on visual inspection of the available optical imaging. These are indicated in the `notes` field of the cluster catalog. Figure 24 shows some examples of both known lenses and new candidates.

5.2.3. Systems with Active or Star-forming Central Galaxies

We flagged 14 systems as potentially hosting central AGNs or significant star formation, purely on the basis of their

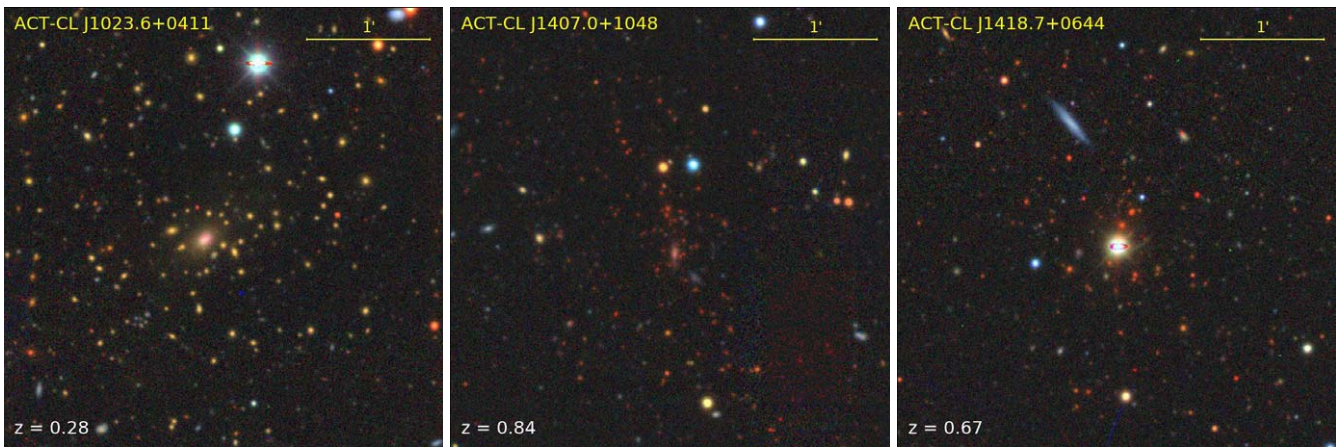


Figure 25. Examples of systems with activity in the cluster core (star formation or possible AGNs; see Section 5.2.3). Each image is $3/5$ on a side, with north at the top and east at the left. ACT-CL J1023.6+0411 is the well-known $z = 0.29$ cool core ZwCl 3146 cluster; ACT-CL J1407.0+1048 is the second ranked cluster in the sample at $z > 0.8$ in terms of S/N, and perhaps has a starburst galaxy in its core; ACT-CL J1418.7+0644 is a high-significance detection by ACT, but it was previously rejected as a false detection in the X-ray cluster catalog of Vikhlinin et al. (1998).

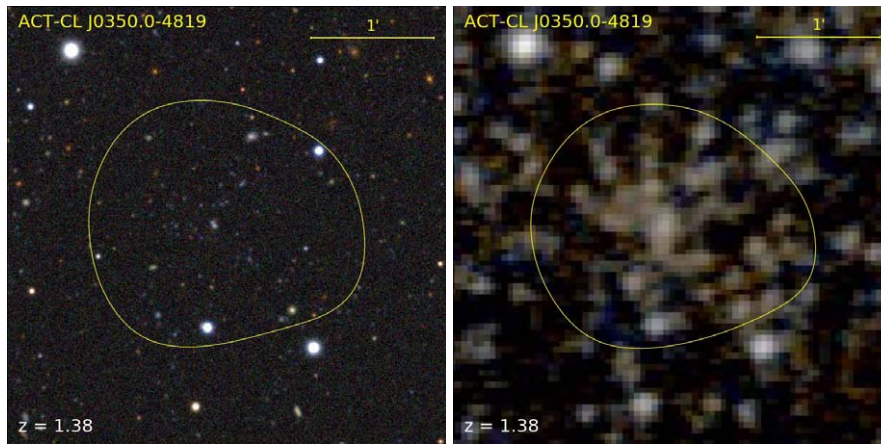


Figure 26. Newly discovered high-redshift cluster ACT-CL J0350.0-4819 at $z = 1.38$. The left panel shows the DES Y3 *gri* optical image, which shows a striking number of blue galaxies within the yellow SZ S/N contour. The right panel shows the WISE IR imaging, demonstrating that the cluster itself is a genuine high-redshift system.

Table 3
Strong Lens Catalogs

Code	Reference
M16	More et al. (2016)
D17	Diehl et al. (2017)
S18	Sonnenfeld et al. (2018)
W18	Wong et al. (2018)
P19	Petrillo et al. (2019)
J19	Jacobs et al. (2019a)
J19a	Jacobs et al. (2019b)
H20a	Huang et al. (2020b)
H20b	Huang et al. (2020c)
Jae20	Jaelani et al. (2020)
D20	H. T. Diehl et al. (2020, in preparation)

Note. Entries in the `knownLensRefCode` column of the cluster catalog (see Table 1) correspond to the Code column used here.

appearance in the available optical/IR imaging, including the well-known cool core cluster ZwCl 3146 (ACT-CL J1023.6+0411) at $z = 0.29$ (e.g., Romero et al. 2020). One of our highest significance detections at $z > 0.8$ is a new cluster in this category, ACT-CL J1407.0+1048 ($z = 0.84$, $S/N_{2.4} = 33.8$, $M_{500c}^{\text{Cal}} = (9.1_{-1.5}^{+1.7}) \times 10^{14} M_{\odot}$), which has a blue BCG as

shown in the DECaLS image (Figure 25). This cluster may have properties similar to the Phoenix cluster (McDonald et al. 2012), but follow-up at other wavelengths is needed to confirm this. Some objects in this category may be “quasars masquerading as clusters” as identified at X-ray wavelengths (Somboonpanyakul et al. 2018; Donahue et al. 2020), after further investigation. For example, ACT-CL J1418.7+0644 (pictured in Figure 25) is detected with $S/N_{2.4} = 12.7$ in the ACT DR5 catalog but was rejected as a false detection in the X-ray cluster catalog of Vikhlinin et al. (1998).

5.2.4. A Blue, High-redshift Galaxy Cluster?

Figure 26 shows optical and WISE IR imaging of the newly discovered $z = 1.38$ cluster ACT-CL J0350.0-4819. The photometric redshift of this system was determined using DECaLS photometry (see Section 3.1.4), and we lack any spectroscopic information. Nevertheless, there is an apparent overdensity of galaxies with blue colors at the cluster position, as seen in the DES *gri* optical image. If this is not simply projection along the line of sight, then it may be that this system hosts an unusually large number of star-forming galaxies. We intend to obtain follow-up spectroscopy of this system to determine if this is in fact the case. ACT-CL J0350.0-4819 is also detected by the

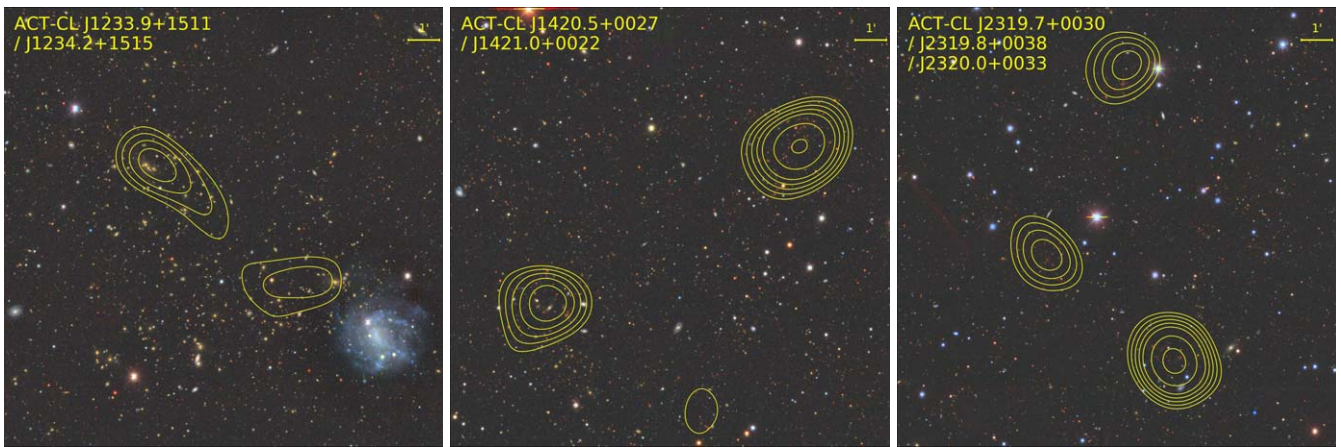


Figure 27. Example DECaLS *grz* images of multiple systems (see Section 5.2.5): ACT-CL J1233.9+1511/J1234.2+1515 at $z = 0.29$ (possibly a pre- or postmerger system); ACT-CL J1420.5+0027/J1421.0+0022 at $z = 0.64$ (two clusters separated by 3.6 Mpc); and the $z = 0.90$ triple system ACT-CL J2319.7+0030/J2319.8+0038/J2320.0+0033 (the RCS2 supercluster; Gilbank et al. 2008). Each image is $13'$ on a side, with north at the top and east at the left. The lowest contour level shown corresponds to 3σ significance in the filtered ACT map. The difference between levels increases by 0.5σ ($3 < S/N < 5$), 1σ ($5 < S/N < 10$), and 2σ ($10 < S/N < 20$).

Table 4
Systems of Multiple SZ Sources

Name	Mean z	Separation (Mpc)	Photo- z ?
ACT-CL J0000.7+0225/J2359.5+0208	0.43	8.1	...
ACT-CL J0003.0–3520/J0003.8–3517	0.76	4.1	✓
ACT-CL J0005.0+0212/J0005.7+0222	0.84	7.0	✓
ACT-CL J0018.3+1618/J0018.5+1626	0.55	3.3	...
ACT-CL J0019.6+0336/J0020.0+0351	0.27	4.0	✓

Note. Only a subset of the available fields in this catalog are shown here. (This table is available in its entirety in FITS format.)

Wavelet Z Photometric optical cluster-finding algorithm (WaZP; M. Aguena et al. 2020, in preparation, presents a catalog based on DES Y1) in a preliminary search of the DES Y6 data. WaZP does not assume a red-sequence model and searches for clusters as spatial overdensities using photometric redshifts.

5.2.5. Multiple Systems

We conducted a search for pairs or groups of clusters in the catalog that may be physically associated. These objects may be of interest for those studying cluster mergers, filaments and large-scale structure around clusters, and superclusters. We select candidates for this category as objects that have a neighboring SZ source within a projected distance of 10 Mpc and a peculiar velocity difference of $< 5000 \text{ km s}^{-1}$. We find a total of 160 such systems, consisting of 144 pairs, 15 triples, and one quadruple system, which are listed in Table 4. Note, however, that some clusters are part of more than one system (e.g., the $z = 0.49$ triple system ACT-CL J0059.6+1310/J0059.8+1344/J0059.9+1319 is also listed as the pairs ACT-CL J0059.6+1310/J0059.9+1319 and ACT-CL J0059.8+1344/J0059.9+1319). We also include objects with photometric redshifts in this search but flag these in the catalog, since the uncertainties on these redshifts are much larger than spectroscopic redshift errors.

We find multiple systems across the redshift range $0.04 < z < 1.2$ (median $z = 0.42$), and the average maximum projected separation between the components of these systems

is 5.8 Mpc. Figure 27 shows a few examples. Due to the increased depth of the ACT DR5 maps, we now detect all three components of the $z = 0.9$ RCS2 supercluster (Gilbank et al. 2008, recorded here as ACT-CL J2319.7+0030/J2319.8+0038/J2320.0+0033). Some of these systems may be pre- or postmerger systems (e.g., ACT-CL J1233.9+1511/J1234.2+1515 at $z = 0.29$, shown in Figure 27).

6. Summary

This work presents the first cluster catalog derived from 98 and 150 GHz observations with the AdvACT receiver, covering a search area of $13,211 \text{ deg}^2$. The catalog contains 4195 optically confirmed galaxy clusters with redshift and mass estimates, making it the largest SZ-selected cluster catalog to date. It is more than 22 times larger than the previous ACT cluster catalog (Hilton et al. 2018), illustrating the huge gains in sensitivity and survey speed achieved by the upgraded AdvACT receiver (Henderson et al. 2016). Assuming a relation between SZ signal and mass calibrated from X-ray observations (Arnaud et al. 2010), the 90% completeness limit of the survey for $S/N_{2.4} > 5$ is $M_{500c} > 3.8 \times 10^{14} M_{\odot}$.

Thanks to the overlap with deep and wide optical surveys like DES (Abbott et al. 2018), DECaLS (Dey et al. 2019), HSC-SSP (Aihara et al. 2018), KiDS (Wright et al. 2019), and SDSS (Ahumada et al. 2020), the optical follow-up of the survey is complete over much of the survey area. The cluster sample has median $z = 0.52$ and covers the redshift range $0.04 < z < 1.91$, with 222 $z > 1$ systems and 868 newly discovered clusters. In the regions that overlap DES Y3, HSC S19A, and KiDS DR4, 95%–98% of the candidates detected with $S/N_{2.4} > 6$ have been confirmed as clusters.

The cluster and source detection package developed for this work is capable of analyzing the next generation of deep, wide multifrequency millimeter-wave maps that will be produced by experiments such as the Simons Observatory (Ade et al. 2019). It will be made publicly available at <https://github.com/simonsobs/nemo/> and on the Python Package Index (PyPI) under a free software license.

ACT was supported by the U.S. National Science Foundation through awards AST-0408698, AST-0965625, and AST-

1440226 for the ACT project, as well as awards PHY-0355328, PHY-0855887, and PHY-1214379. Funding was also provided by Princeton University, the University of Pennsylvania, and a Canada Foundation for Innovation (CFI) award to UBC. ACT operates in the Parque Astronómico Atacama in northern Chile under the auspices of the Comisión Nacional de Investigación (CONICYT). The development of multichroic detectors and lenses was supported by NASA grants NNX13AE56G and NNX14AB58G. Detector research at NIST was supported by the NIST Innovations in Measurement Science program.

C.S. acknowledges support from the Agencia Nacional de Investigación y Desarrollo through FONDECYT Iniciación grant No. 11191125. S.K.C. acknowledges support from the Cornell Presidential Postdoctoral Fellowship. R.D. thanks CONICYT for grant BASAL CATA AFB-170002. Z.L., E. S., and J.D. are supported through NSF grant AST-1814971. K. M. and M.Hi. acknowledge support from the National Research Foundation of South Africa (grant No. 112132). M.D.N. acknowledges support from NSF award AST-1454881. D.H., A.M., and N.S. acknowledge support from NSF grant Nos. AST-1513618 and AST-1907657. E.C. acknowledges support from the STFC Ernest Rutherford Fellowship ST/M004856/2 and STFC Consolidated Grant ST/S00033X/1, and from the Horizon 2020 ERC Starting Grant (grant agreement No. 849169). N.B. acknowledges support from NSF grant AST-1910021. M.L. was supported by a Dicke Fellowship. L.P. acknowledges support from the Mishrahi and Wilkinson funds. A.J. acknowledges support from JSPS KAKENHI grant No. JP17H02868. J.P.H. acknowledges funding for SZ cluster studies from NSF grant No. AST-1615657. R.D. thanks CONICYT for grant BASAL CATA AFB-170002. The Flatiron Institute is supported by the Simons Foundation. Computations were performed on Hippo at the University of KwaZulu-Natal.

Funding for the DES Projects has been provided by the DOE and NSF (USA), MEC/MICINN/MINECO (Spain), STFC (UK), HEFCE (UK), NCSA (UIUC), KICP (U. Chicago), CCAPP (Ohio State), MIFPA (Texas A&M), CNPQ, FAPERJ, FINEP (Brazil), DFG (Germany), and the Collaborating Institutions in the Dark Energy Survey.

The Collaborating Institutions are Argonne Lab, UC Santa Cruz, University of Cambridge, CIEMAT-Madrid, University of Chicago, University College London, DES-Brazil Consortium, University of Edinburgh, ETH Zürich, Fermilab, University of Illinois, ICE (IEEC-CSIC), IFAE Barcelona, Lawrence Berkeley Lab, LMU München and the associated Excellence Cluster Universe, University of Michigan, NFS's NOIRLab, University of Nottingham, Ohio State University, University of Pennsylvania, University of Portsmouth, SLAC National Lab, Stanford University, University of Sussex, Texas A&M University, and the OzDES Membership Consortium.

This work is based in part on observations at Cerro Tololo Inter-American Observatory at NSF's NOIRLab (NOIRLab Prop. ID 2012B-0001; PI: J. Frieman), which is managed by the Association of Universities for Research in Astronomy (AURA) under a cooperative agreement with the National Science Foundation.

The DES Data Management System is supported by the NSF under Grant Nos. AST-1138766 and AST-1536171. The DES participants from Spanish institutions are partially supported by MICINN under grants ESP2017-89838, PGC2018-094773, PGC2018-102021, SEV-2016-0588, SEV-2016-0597, and

MDM-2015-0509, some of which include ERDF funds from the European Union. IFAE is partially funded by the CERCA program of the Generalitat de Catalunya. Research leading to these results has received funding from the European Research Council under the European Union's Seventh Framework Program (FP7/2007-2013) including ERC grant agreements 240672, 291329, and 306478. We acknowledge support from the Brazilian Instituto Nacional de Ciência e Tecnologia (INCT) do e-Universo (CNPq grant 465376/2014-2).

This manuscript has been authored by Fermi Research Alliance, LLC under Contract No. DE-AC02-07CH11359 with the U.S. Department of Energy, Office of Science, Office of High Energy Physics.

The Hyper Suprime-Cam (HSC) collaboration includes the astronomical communities of Japan and Taiwan and Princeton University. The HSC instrumentation and software were developed by the National Astronomical Observatory of Japan (NAOJ), the Kavli Institute for the Physics and Mathematics of the Universe (Kavli IPMU), the University of Tokyo, the High Energy Accelerator Research Organization (KEK), the Academia Sinica Institute for Astronomy and Astrophysics in Taiwan (ASIAA), and Princeton University. Funding was contributed by the FIRST program from the Japanese Cabinet Office, the Ministry of Education, Culture, Sports, Science and Technology (MEXT), the Japan Society for the Promotion of Science (JSPS), the Japan Science and Technology Agency (JST), the Toray Science Foundation, NAOJ, Kavli IPMU, KEK, ASIAA, and Princeton University.

This paper makes use of software developed for the Rubin Observatory. We thank the Rubin Observatory Project for making their code available as free software at <http://dm.lsst.org>.

This paper is based in part on data collected at the Subaru Telescope and retrieved from the HSC data archive system, which is operated by Subaru Telescope and Astronomy Data Center (ADC) at NAOJ. Data analysis was in part carried out with the cooperation of the Center for Computational Astrophysics (CfCA), NAOJ.

The Pan-STARRS1 Surveys (PS1) and the PS1 public science archive have been made possible through contributions by the Institute for Astronomy, the University of Hawaii, the Pan-STARRS Project Office, the Max Planck Society and its participating institutes, the Max Planck Institute for Astronomy, Heidelberg, and the Max Planck Institute for Extraterrestrial Physics, Garching, The Johns Hopkins University, Durham University, the University of Edinburgh, the Queen's University Belfast, the Harvard-Smithsonian Center for Astrophysics, the Las Cumbres Observatory Global Telescope Network Incorporated, the National Central University of Taiwan, the Space Telescope Science Institute, the National Aeronautics and Space Administration under grant No. NNX08AR22G issued through the Planetary Science Division of the NASA Science Mission Directorate, the National Science Foundation grant No. AST-1238877, the University of Maryland, Eotvos Lorand University (ELTE), the Los Alamos National Laboratory, and the Gordon and Betty Moore Foundation.

The Legacy Surveys consist of three individual and complementary projects: the Dark Energy Camera Legacy Survey (DECaLS; NOAO Proposal ID 2014B-0404; PIs: David Schlegel and Arjun Dey), the Beijing-Arizona Sky Survey (BASS; NOAO Proposal ID 2015A-0801; PIs: Zhou

Xu and Xiaohui Fan), and the Mayall z-band Legacy Survey (MzLS; NOAO Proposal ID 2016A-0453; PI: Arjun Dey). DECaLS, BASS, and MzLS together include data obtained, respectively, at the Blanco telescope, Cerro Tololo Inter-American Observatory, National Optical Astronomy Observatory (NOAO); the Bok telescope, Steward Observatory, University of Arizona; and the Mayall telescope, Kitt Peak National Observatory, NOAO. The Legacy Surveys project is honored to be permitted to conduct astronomical research on Iolkam Du'ag (Kitt Peak), a mountain with particular significance to the Tohono O'odham Nation.

NOAO is operated by the Association of Universities for Research in Astronomy (AURA) under a cooperative agreement with the National Science Foundation.

The Legacy Survey team makes use of data products from the Near-Earth Object Wide-field Infrared Survey Explorer (NEOWISE), which is a project of the Jet Propulsion Laboratory/California Institute of Technology. NEOWISE is funded by the National Aeronautics and Space Administration.

The Legacy Surveys imaging of the DESI footprint is supported by the Director, Office of Science, Office of High Energy Physics of the U.S. Department of Energy under Contract No. DE-AC02-05CH1123; by the National Energy Research Scientific Computing Center, a DOE Office of Science User Facility under the same contract; and by the U.S. National Science Foundation, Division of Astronomical Sciences under Contract No. AST-0950945 to NOAO.

Software: AstroPy (Astropy Collaboration et al. 2013), Core Cosmology Library (Chisari et al. 2019), Pixell (<https://github.com/simonsobs/pixell/>).

ORCID iDs

M. Hilton <https://orcid.org/0000-0002-8490-8117>
 C. Sifón <https://orcid.org/0000-0002-8149-1352>
 M. Madhavacheril <https://orcid.org/0000-0001-6740-5350>
 M. Oguri <https://orcid.org/0000-0003-3484-399X>
 E. Rykoff <https://orcid.org/0000-0001-9376-3135>
 J. Annis <https://orcid.org/0000-0002-0609-3987>
 C. Aros-Bunster <https://orcid.org/0000-0002-9441-3193>
 G. M. Bernstein <https://orcid.org/0000-0002-8613-8259>
 D. Brooks <https://orcid.org/0000-0002-8458-5047>
 M. Carrasco Kind <https://orcid.org/0000-0002-4802-3194>
 J. Carretero <https://orcid.org/0000-0002-3130-0204>
 C. Conselice <https://orcid.org/0000-0003-1949-7638>
 M. Costanzi <https://orcid.org/0000-0001-8158-1449>
 D. Crichton <https://orcid.org/0000-0003-1204-3035>
 S. R. Dicker <https://orcid.org/0000-0002-1940-4289>
 H. T. Diehl <https://orcid.org/0000-0002-8357-7467>
 J. P. Dietrich <https://orcid.org/0000-0002-8134-9591>
 S. Ferraro <https://orcid.org/0000-0003-4992-7854>
 B. Flaugher <https://orcid.org/0000-0002-2367-5049>
 J. Frieman <https://orcid.org/0000-0003-4079-3263>
 J. García-Bellido <https://orcid.org/0000-0002-9370-8360>
 E. Gaztanaga <https://orcid.org/0000-0001-9632-0815>
 D. W. Gerdes <https://orcid.org/0000-0001-6942-2736>
 D. Gruen <https://orcid.org/0000-0003-3270-7644>
 R. A. Gruendl <https://orcid.org/0000-0002-4588-6517>
 J. Gschwend <https://orcid.org/0000-0003-3023-8362>
 G. Gutierrez <https://orcid.org/0000-0003-0825-0517>
 A. D. Hincks <https://orcid.org/0000-0003-1690-6678>
 S. R. Hinton <https://orcid.org/0000-0003-2071-9349>
 K. Honscheid <https://orcid.org/0000-0002-6550-2023>

B. Hoyle <https://orcid.org/0000-0002-2571-1357>
 K. M. Huffenberger <https://orcid.org/0000-0001-7109-0099>
 J. P. Hughes <https://orcid.org/0000-0002-8816-6800>
 D. J. James <https://orcid.org/0000-0001-5160-4486>
 K. Kuehn <https://orcid.org/0000-0003-0120-0808>
 O. Lahav <https://orcid.org/0000-0002-1134-9035>
 M. A. G. Maia <https://orcid.org/0000-0001-9856-9307>
 P. Melchior <https://orcid.org/0000-0002-8873-5065>
 F. Menanteau <https://orcid.org/0000-0002-1372-2534>
 R. Miquel <https://orcid.org/0000-0002-6610-4836>
 K. Moodley <https://orcid.org/0000-0001-6606-7142>
 T. Mroczkowski <https://orcid.org/0000-0003-3816-5372>
 A. J. Nishizawa <https://orcid.org/0000-0002-6109-2397>
 R. L. C. Ogando <https://orcid.org/0000-0003-2120-1154>
 A. Palmese <https://orcid.org/0000-0002-6011-0530>
 A. A. Plazas <https://orcid.org/0000-0002-2598-0514>
 A. K. Romer <https://orcid.org/0000-0002-9328-879X>
 A. Carnero Rosell <https://orcid.org/0000-0003-3044-5150>
 E. Sanchez <https://orcid.org/0000-0002-9646-8198>
 N. Sehgal <https://orcid.org/0000-0002-9674-4527>
 M. Soares-Santos <https://orcid.org/0000-0001-6082-8529>
 D. N. Spergel <https://orcid.org/0000-0002-5151-0006>
 E. Suchyta <https://orcid.org/0000-0002-7047-9358>
 G. Tarle <https://orcid.org/0000-0003-1704-0781>
 C. To <https://orcid.org/0000-0001-7836-2261>
 H. Trac <https://orcid.org/0000-0001-6778-3861>
 J. De Vicente <https://orcid.org/0000-0001-8318-6813>
 E. J. Wollack <https://orcid.org/0000-0002-7567-4451>
 Z. Xu <https://orcid.org/0000-0001-5112-2567>

References

- Abbott, T. M. C., Abdalla, F. B., Allam, S., et al. 2018, *ApJS*, 239, 18
 Abell, G. O., Corwin, H. G. J., & Olowin, R. P. 1989, *ApJS*, 70, 1
 Ade, P., Aguirre, J., Ahmed, Z., et al. 2019, *JCAP*, 2019, 056
 Ahumada, R., Allende Prieto, C., Almeida, A., et al. 2020, *ApJS*, 249, 3
 Aihara, H., Arimoto, N., Armstrong, R., et al. 2018, *PASJ*, 70, S4
 Aiola, S., Calabrese, E., Maurin, L., et al. 2020, arXiv:2007.07288
 Allen, S. W., Rapetti, D. A., Schmidt, R. W., et al. 2008, *MNRAS*, 383, 879
 Allen, S. W., Schmidt, R. W., Ebeling, H., Fabian, A. C., & van Speybroeck, L. 2004, *MNRAS*, 353, 457
 Arnaud, M., Pointecouteau, E., & Pratt, G. W. 2005, *A&A*, 441, 893
 Arnaud, M., Pratt, G. W., Piffaretti, R., et al. 2010, *A&A*, 517, A92
 Astropy Collaboration, Robitaille, T. P., Tollerud, E. J., et al. 2013, *A&A*, 558, A33
 Barkhouse, W. A., Green, P. J., Vikhlinin, A., et al. 2006, *ApJ*, 645, 955
 Battaglia, N., Leauthaud, A., Miyatake, H., et al. 2016, *JCAP*, 8, 013
 Beers, T. C., Flynn, K., & Gebhardt, K. 1990, *AJ*, 100, 32
 Bhattacharya, S., Habib, S., Heitmann, K., & Vikhlinin, A. 2013, *ApJ*, 766, 32
 Birkinshaw, M. 1999, *PhR*, 310, 97
 Blake, C., Amon, A., Childress, M., et al. 2016, *MNRAS*, 462, 4240
 Bleem, L. E., Bocquet, S., Stalder, B., et al. 2020, *ApJS*, 247, 25
 Bleem, L. E., Stalder, B., Brodwin, M., et al. 2015a, *ApJS*, 216, 20
 Bleem, L. E., Stalder, B., de Haan, T., et al. 2015b, *ApJS*, 216, 27
 Bocquet, S., Dietrich, J. P., Schrabback, T., et al. 2019, *ApJ*, 878, 55
 Böhringer, H., Schuecker, P., Guzzo, L., et al. 2004, *A&A*, 425, 367
 Böhringer, H., Voges, W., Huchra, J. P., et al. 2000, *ApJS*, 129, 435
 Bradley, L. D., Zitrin, A., Coe, D., et al. 2014, *ApJ*, 792, 76
 Brammer, G. B., van Dokkum, P. G., & Coppi, P. 2008, *ApJ*, 686, 1503
 Bruzual, G., & Charlot, S. 2003, *MNRAS*, 344, 1000
 Buddendiek, A., Schrabback, T., Greer, C. H., et al. 2015, *MNRAS*, 450, 4248
 Burenin, R. A., Vikhlinin, A., Hornstrup, A., et al. 2007, *ApJS*, 172, 561
 Caccianiga, A., Maccacaro, T., Wolter, A., Della Ceca, R., & Gioia, I. M. 2000, *A&AS*, 144, 247
 Calabretta, M. R., & Greisen, E. W. 2002, *A&A*, 395, 1077
 Cappi, A., Held, E. V., & Marano, B. 1998, *A&AS*, 129, 31
 Carlstrom, J. E., Holder, G. P., & Reese, E. D. 2002, *ARA&A*, 40, 643
 Cavagnolo, K. W., Donahue, M., Voit, G. M., & Sun, M. 2008, *ApJ*, 682, 821
 Childress, M. J., Lidman, C., Davis, T. M., et al. 2017, *MNRAS*, 472, 273
 Chisari, N. E., Alonso, D., Krause, E., et al. 2019, *ApJS*, 242, 2

- Choi, S. K., Austermann, J., Beall, J. A., et al. 2018, *JLTP*, 193, 267
- Choi, S. K., Hasselfield, M., Ho, S.-P. P., et al. 2020, arXiv:2007.07289
- Chon, G., & Böhringer, H. 2012, *A&A*, 538, A35
- Coleman, G. D., Wu, C.-C., & Weedman, D. W. 1980, *ApJS*, 43, 393
- Connor, T., Kelson, D. D., Blanc, G. A., & Boutsia, K. 2019, *ApJ*, 878, 66
- Coziol, R., Andernach, H., Caretta, C. A., Alamo-Martínez, K. A., & Tago, E. 2009, *AJ*, 137, 4795
- Crawford, C. S., Edge, A. C., Fabian, A. C., et al. 1995, *MNRAS*, 274, 75
- Crawford, S. M., Wirth, G. D., & Bershad, M. A. 2014, *ApJ*, 786, 30
- Crudace, R., Voges, W., Böhringer, H., et al. 2002, *ApJS*, 140, 239
- Dalton, G. B., Efstathiou, G., Maddox, S. J., & Sutherland, W. J. 1994, *MNRAS*, 269, 151
- Dawson, K. S., Aldering, G., Amanullah, R., et al. 2009, *AJ*, 138, 1271
- De Grandi, S., Böhringer, H., Guzzo, L., et al. 1999, *ApJ*, 514, 148
- De Propriis, R., Couch, W. J., Colless, M., et al. 2002, *MNRAS*, 329, 87
- Dey, A., Schlegel, D. J., Lang, D., et al. 2019, *AJ*, 157, 168
- Diehl, H. T., Buckley-Geer, E. J., Lindgren, K. A., et al. 2017, *ApJS*, 232, 15
- Donahue, M., Funkhouser, K., Koeppe, D., Frisbie, R. L. S., & Voit, G. M. 2020, *ApJ*, 889, 121
- Dünner, R., Hasselfield, M., Marriage, T. A., et al. 2013, *ApJ*, 762, 10
- Durret, F., Adami, C., Cappi, A., et al. 2011, *A&A*, 535, A65
- Ebeling, H., Barrett, E., Donovan, D., et al. 2007, *ApJL*, 661, L33
- Edge, A., Sutherland, W., Kuijken, K., et al. 2013, *Msngr*, 154, 32
- Ehler, S., Allen, S. W., Brandt, W. N., et al. 2015, *MNRAS*, 446, 2709
- Fassbender, R., Böhringer, H., Santos, J. S., et al. 2011, *A&A*, 527, A78
- Flewelling, H. A., Magnier, E. A., Chambers, K. C., et al. 2016, arXiv:1612.05243
- Fowler, J. W., Niemack, M. D., Dicker, S. R., et al. 2007, *ApOpt*, 46, 3444
- Gal, R. R., Lopes, P. A. A., de Carvalho, R. R., et al. 2009, *AJ*, 137, 2981
- Geach, J. E., Murphy, D. N. A., & Bower, R. G. 2011, *MNRAS*, 413, 3059
- Gilbank, D. G., Yee, H. K. C., Ellingson, E., et al. 2008, *ApJL*, 677, L89
- Gioia, I. M., & Luppino, G. A. 1994, *ApJS*, 94, 583
- Gladders, M. D., Hoekstra, H., Yee, H. K. C., Hall, P. B., & Barrientos, L. F. 2003, *ApJ*, 593, 48
- Gonzalez, A. H., Decker, B., Brodwin, M., et al. 2015, *ApJL*, 812, L40
- Gonzalez, A. H., Gettings, D. P., Brodwin, M., et al. 2019, *ApJS*, 240, 33
- Goto, T., Sekiguchi, M., Nichol, R. C., et al. 2002, *AJ*, 123, 1807
- Gralla, M. B., Sharon, K., Gladders, M. D., et al. 2011, *ApJ*, 737, 74
- Hasselfield, M., Hilton, M., Marriage, T. A., et al. 2013, *JCAP*, 7, 8
- Henderson, S. W., Allison, R., Austermann, J., et al. 2016, *JLTP*, 184, 772
- Hilton, M., Hasselfield, M., Sifón, C., et al. 2018, *ApJS*, 235, 20
- Ho, S.-P. P., Austermann, J., Beall, J. A., et al. 2017, *Proc. SPIE*, 9914, 991418
- Hoekstra, H., Herbonnet, R., Muzzin, A., et al. 2015, *MNRAS*, 449, 685
- Huang, N., Bleem, L. E., Stalder, B., et al. 2020a, *AJ*, 159, 110
- Huang, X., Storfer, C., Gu, A., et al. 2020c, arXiv:2005.04730
- Huang, X., Storfer, C., Ravi, V., et al. 2020b, *ApJ*, 894, 78
- Hughes, J. P., Birkinshaw, M., & Huchra, J. P. 1995, *ApJL*, 448, L93
- Ilbert, O., Capak, P., Salvato, M., et al. 2009, *ApJ*, 690, 1236
- Itoh, N., Kohyama, Y., & Nozawa, S. 1998, *ApJ*, 502, 7
- Jacobs, C., Collett, T., Glazebrook, K., et al. 2019a, *MNRAS*, 484, 5330
- Jacobs, C., Collett, T., Glazebrook, K., et al. 2019b, *ApJS*, 243, 17
- Jaelani, A. T., More, A., Oguri, M., et al. 2020, *MNRAS*, 495, 1291
- Klein, M., Grandis, S., Mohr, J. J., et al. 2019, *MNRAS*, 488, 739
- Lauer, T. R., Postman, M., Strauss, M. A., Graves, G. J., & Chisari, N. E. 2014, *ApJ*, 797, 82
- Lopes, P. A. A., de Carvalho, R. R., Gal, R. R., et al. 2004, *AJ*, 128, 1017
- Madhavacheril, M. S., Hill, J. C., Naess, S., et al. 2020, *PhRvD*, 102, 023534
- Mann, A. W., & Ebeling, H. 2012, *MNRAS*, 420, 2120
- Mantz, A., Allen, S. W., Ebeling, H., Rapetti, D., & Drlica-Wagner, A. 2010, *MNRAS*, 406, 1773
- Mantz, A. B., Abdulla, Z., Allen, S. W., et al. 2018, *A&A*, 620, A2
- Mantz, A. B., Abdulla, Z., Carlstrom, J. E., et al. 2014, *ApJ*, 794, 157
- Marriage, T. A., Acquaviva, V., Ade, P. A. R., et al. 2011, *ApJ*, 737, 61
- Maturi, M., Bellagamba, F., Radovich, M., et al. 2019, *MNRAS*, 485, 498
- McClintock, T., Varga, T. N., Gruen, D., et al. 2019, *MNRAS*, 482, 1352
- McDonald, M., Bayliss, M., Benson, B. A., et al. 2012, *Natur*, 488, 349
- Medezinski, E., Battaglia, N., Umetsu, K., et al. 2018, *PASJ*, 70, 528
- Mehrtens, N., Romer, A. K., Hilton, M., et al. 2012, *MNRAS*, 423, 1024
- Melin, J. B., Bartlett, J. G., & Delabrouille, J. 2006, *A&A*, 459, 341
- Menanteau, F., Sifón, C., Barrientos, L. F., et al. 2013, *ApJ*, 765, 67
- Menanteau, F., González, J., Juin, J.-B., et al. 2010, *ApJ*, 723, 1523
- Miyatake, H., Battaglia, N., Hilton, M., et al. 2019, *ApJ*, 875, 63
- Miyazaki, S., Komiyama, Y., Kawanomoto, S., et al. 2018, *PASJ*, 70, S1
- More, A., Verma, A., Marshall, P. J., et al. 2016, *MNRAS*, 455, 1191
- Mroczkowski, T., Nagai, D., Basu, K., et al. 2019, *SSRv*, 215, 17
- Mullis, C. R., McNamara, B. R., Quintana, H., et al. 2003, *ApJ*, 594, 154
- Murphy, D. N. A., Geach, J. E., & Bower, R. G. 2012, *MNRAS*, 420, 1861
- Naess, S., Aiola, S., Austermann, J. E., et al. 2020, arXiv:2007.07290
- Nastasi, A., Böhringer, H., Fassbender, R., et al. 2014, *A&A*, 564, A17
- Oegerle, W. R., & Hill, J. M. 2001, *AJ*, 122, 2858
- Oguri, M. 2014, *MNRAS*, 444, 147
- Oguri, M., Lin, Y.-T., Lin, S.-C., et al. 2018, *PASJ*, 70, S20
- Oke, J. B. 1974, *ApJS*, 27, 21
- Petrillo, C. E., Tortora, C., Varnardos, G., et al. 2019, *MNRAS*, 484, 3879
- Pimblett, C. L., Smail, I., Edge, A. C., et al. 2006, *MNRAS*, 366, 645
- Planck Collaboration, Ade, P. A. R., Aghanim, N., et al. 2014a, *A&A*, 571, A20
- Planck Collaboration, Ade, P. A. R., Aghanim, N., et al. 2014b, *A&A*, 571, A29
- Planck Collaboration, Ade, P. A. R., Aghanim, N., et al. 2015, *A&A*, 582, A29
- Planck Collaboration, Ade, P. A. R., Aghanim, N., et al. 2016a, *A&A*, 594, A24
- Planck Collaboration, Ade, P. A. R., Aghanim, N., et al. 2016b, *A&A*, 594, A27
- Planck Collaboration, Aghanim, N., Arnaud, M., et al. 2012, *A&A*, 543, A102
- Proust, D., Yegorova, I., Saviane, I., et al. 2015, *MNRAS*, 452, 3304
- Reichardt, C. L., Stalder, B., Bleem, L. E., et al. 2013, *ApJ*, 763, 127
- Romer, A. K., Nichol, R. C., Holden, B. P., et al. 2000, *ApJS*, 126, 209
- Romero, C. E., Sievers, J., Ghirardini, V., et al. 2020, *ApJ*, 891, 90
- Rykoff, E. S., Roza, E., Busha, M. T., et al. 2014, *ApJ*, 785, 104
- Rykoff, E. S., Roza, E., Hollowood, D., et al. 2016, *ApJS*, 224, 1
- Salvato, M., Ilbert, O., Hasinger, G., et al. 2011, *ApJ*, 742, 61
- Schmidt, R. W., & Allen, S. W. 2007, *MNRAS*, 379, 209
- Schweppe, A., Hasinger, G., Lehmann, I., et al. 2000, *AN*, 321, 1
- Scoddeggio, M., Guzzo, L., Garilli, B., et al. 2018, *A&A*, 609, A84
- Sehgal, N., Trac, H., Acquaviva, V., et al. 2011, *ApJ*, 732, 44
- Sereni, M. 2015, *MNRAS*, 450, 3665
- Sharon, K., Gal-Yam, A., Maoz, D., et al. 2010, *ApJ*, 718, 876
- Shectman, S. A., Landy, S. D., Oemler, A., et al. 1996, *ApJ*, 470, 172
- Sifón, C., Battaglia, N., Hasselfield, M., et al. 2016, *MNRAS*, 461, 248
- Simet, M., McClintock, T., Mandelbaum, R., et al. 2017, *MNRAS*, 466, 3103
- Smith, G. P., Mazzotta, P., Okabe, N., et al. 2016, *MNRAS*, 456, L74
- Smith, R. J., Hudson, M. J., Nelan, J. E., et al. 2004, *AJ*, 128, 1558
- Somboonpanyakul, T., McDonald, M., Lin, H. W., Stalder, B., & Stark, A. 2018, *ApJ*, 863, 122
- Song, J., Zenteno, A., Stalder, B., et al. 2012, *ApJ*, 761, 22
- Sonnenfeld, A., Chan, J. H. H., Shu, Y., et al. 2018, *PASJ*, 70, S29
- Stanford, S. A., Gonzalez, A. H., Brodwin, M., et al. 2014, *ApJS*, 213, 25
- Staniszewski, Z., Ade, P. A. R., Aird, K. A., et al. 2009, *ApJ*, 701, 32
- Stein, G., Alvarez, M. A., Bond, J. R., van Engelen, A., & Battaglia, N. 2020, arXiv:2001.08787
- Stocke, J. T., Morris, S. L., Gioia, I. M., et al. 1991, *ApJS*, 76, 813
- Struble, M. F., & Rood, H. J. 1991, *ApJS*, 77, 363
- Struble, M. F., & Rood, H. J. 1999, *ApJS*, 125, 35
- Sunyaev, R. A., & Zel'dovich, Y. B. 1970, *CoASP*, 2, 66
- Sunyaev, R. A., & Zel'dovich, Y. B. 1972, *CoASP*, 4, 173
- Swetz, D. S., Ade, P. A. R., Amiri, M., et al. 2011, *ApJS*, 194, 41
- Thornton, R. J., Ade, P. A. R., Aiola, S., et al. 2016, *ApJS*, 227, 21
- Tinker, J., Kravtsov, A. V., Klypin, A., et al. 2008, *ApJ*, 688, 709
- Tucker, W., Blanco, P., Rappoport, S., et al. 1998, *ApJL*, 496, L5
- Valtchanov, I., Pierre, M., Willis, J., et al. 2004, *A&A*, 423, 75
- Vanderlinde, K., Crawford, T. M., de Haan, T., et al. 2010, *ApJ*, 722, 1180
- Vikhlinin, A., McNamara, B. R., Forman, W., et al. 1998, *ApJ*, 502, 558
- von der Linden, A., Mantz, A., Allen, S. W., et al. 2014, *MNRAS*, 443, 1973
- Wen, Z. L., & Han, J. L. 2015, *ApJ*, 807, 178
- Wen, Z. L., Han, J. L., & Liu, F. S. 2012, *ApJS*, 199, 34
- White, D. A. 2000, *MNRAS*, 312, 663
- Williamson, R., Benson, B. A., High, F. W., et al. 2011, *ApJ*, 738, 139
- Willis, J. P., Clerc, N., Bremer, M. N., et al. 2013, *MNRAS*, 430, 134
- Wong, K. C., Sonnenfeld, A., Chan, J. H. H., et al. 2018, *ApJ*, 867, 107
- Wright, A. H., Hildebrandt, H., Kuijken, K., et al. 2019, *A&A*, 632, A34
- Wright, E. L., Eisenhardt, P. R. M., Mainzer, A. K., et al. 2010, *AJ*, 140, 1868
- Wuyts, E., Barrientos, L. F., Gladders, M. D., et al. 2010, *ApJ*, 724, 1182
- Zaritsky, D., Gonzalez, A. H., & Zabludoff, A. I. 2006, *ApJ*, 638, 725